Politecnico di Torino

POLITECNICO DI TORINO

Mechanical & Aerospace Engineering Department

DIMEAS

Master's Degree Course in Mechanical Engineering

A/Y 2022/2023

Simulation of the mechanical behavior of lattice structure components with a multiscale approach

Supervisor:

Prof. Andrea Tridello

Candidate:

Leonardo Ferrali

Co-supervisors:

Prof. Alberto Ciampaglia

Prof. Carlo Boursier Niutta

Prof. Davide Salvatore Paolino

Abstract

With the development of Additive Manufacturing, it has become possible to create components with complex geometries, such as lattice or reticular structures. Thanks to their high specific energy absorption combined with low mass, these structures have proven to be very interesting in terms of mechanical properties.

The aim of this thesis is to create a numerical model that allows estimating the mechanical behavior of 3D printed components with lattice structures using a multiscale approach. Micro Computer Technology analyses performed on AlSi10Mg lattice specimens revealed the presence of internal porosity within the lattice structure.

To account for these internal defects, a multiscale approach was adopted, allowing for faster and more precise simulations at the microscopic level with three-dimensional elements incorporating defects, using Abaqus CAE for Finite Element Analysis. Equivalent mechanical properties were obtained and extended to the macroscopic level of the component. LS-Dyna software was then used to perform simulations directly on the lattice specimen, associating the mechanical characteristics obtained at the microscale with each 1D element of the mesh.

The Stress-Strain curves obtained at the microscale, by randomly introducing defects into the structure, resulted in a variability of mechanical response in the lattice specimen. Subsequently, the lattice specimen underwent a quasi-static compression test, yielding a force-displacement response.

The family of numerical curves generated from the multiscale Finite Element Analysis allowed for the creation of a band that contained the experimental curve, thus accurately simulating the mechanical behavior of the lattice structure and validating the numerical model.

Summary

1 Introduction 1

1.1 Lattice structure 1

1.2 Multiscale method 5

2 Thesis objective 7

3 Experimental analysis 9

3.1 Material characteristics 9

3.2 Experimental tests 10

3.2.1 Specimens geometry 11

3.2.2 Compression test 11

3.2.3 Nano – indentation test 16

3.3 Internal defects 18

4 Representation of the model using a multiscale method 26

4.1 Multiscale analysis with cubic RVE 30

4.1.1 Model geometry 30

4.1.2 Boundary conditions 31

4.1.3 Definition of the displacement and constraint 34

4.1.4 FE simulations on the RVE 36

4.1.5 Analysis of the results 43

4.2 Multiscale analysis with cylindrical RVE 52

4.2.1 Model geometry 52

4.2.2 Boundary conditions 53

4.2.3 FE simulations 54

5 FEA Modeling of the influence of defects 59

6 Finite Element Analysis on the specimen 72

Conclusions 89

References 94

Aknowledgements 96

Ringraziamenti 97

List of Figures

Figure 1.1. Example of lattice structures produced with AM technologies [1] 2
Figure 1.2. Examples of unit cell configurations for lattice structures. The octlet cell is the second from the bottom [3] 4
Figure 1.3. Multiscale approach: homogenization and localization techniques [5] 6
Figure 3.1. Experimental engineering stress-strain curve of the AlSi10Mg lattice specimen 10
Figure 3.2 Clamped-guided (CG) configuration of the specimen during the compression test 12
Figure 3.3 The machine used for the compression test: Instron 8801 13
Figure 3.4 Image of the specimen in the machine acquired by the optical microscope . 14
Figure 3.5 Image of the specimen undergoing a compression test, with the occurrence of buckling 14
Figure 3.6 Comparison of stress-strain curves between the reference AlSi10Mg alloy (red curve) and that obtained from the quasi-static compression test on a new AlSi10Mg specimen (blue curve) 16
Figure 3.7 Elastic modulus values as a function of penetration depth, for various measurements 18
Figure 3.8 Lattice structure specimen made of AlSi10Mg aluminum alloy undergoing compression testing 19
Figure 3.9 Images of the specimen surface captured by the scanning electron microscope 20
Figure 3.10 Three-dimensional reconstruction of a specimen based on the grayscale... 21
Figure 3.11 View on the XY plane of a scan, with a focus on an internal spherical defect at the intersection of two structural beams 21
Figure 3.12 Probability distribution of the defects in the 20 x 20 x 20 mm specimen for each size 22
Figure 3.13. Probability distribution of the defects in the 30 x 30 x 30 mm specimen for each size 23
Figure 4.1 Comparison between the nominal curve of AlSi10Mg and the curve of AlSi10Mg manufactured through Additive Manufacturing (AM) for lattice structure. The new elastic modulus determined from nanoindentation tests is 53000 MPa 27
Figure 4.2 RVE model with internal spherical defect created in Abaqus CAE 30
Figure 4.3 RVE model with 3D Tetra mesh 33
Figure 4.4 Periodic boundary conditions on the RVE and focus on the nodes of a single equation 34

Figure 4.5 Imposition of a fixed constraint on a vertex and displacement at the dummy node 35
Figure 4.6. Parametrization of the displacement at the dummy node 36
Figure 4.7. Finite Element Analysis (FEA) results: deformation induced on the RVE ... 41
Figure 4.8. Stress concentration between two elements due to mesh errors 42
Figure 4.9. Stress distribution after setting a minimum and maximum value in the contour plot 43
Figure 4.10. Stress and strain data, elastic modulus value obtained from the ODB file 44
Figure 4.11. Count of elements at failure in the model 44
Figure 4.12. Convergence of the elastic modulus for FEA simulations 45
Figure 4.13. Trend of curves with internal defects for fixed-side RVEs with a side length of 1.31 mm. The green curve represents the experimental data of the specimen 47
Figure 4.14. Stress-strain curve variabile RVE: reduction of the ultimate strain for each curve when at least 10% of the elements reach failure 48
Figure 4.15. Stress-strain curve variabile RVE: new family of curves obtained with the updated class distribution 51
Figure 4.16 3D beam model with an internal spherical cavity created in Abaqus CAE 52
Figure 4.17 Creating rigid interaction with the face nodes and defining displacement boundary conditions 53
Figure 4.18 Deformed configuration of the beam with a contour plot of strain E11 54
Figure 4.19 Deformed configuration of the beam with a contour plot of stress S11 55
Figure 4.20 First element to fail within the beam near the spherical cavity 56
Figure 4.21 Variation of maximum stress with respect to the failure threshold of elements 56
Figure 4.22 Distribution of σ-ε curves obtained using local-scale 3D cylindrical elements 57
Figure 5.1. 3D model of the lattice specimen type 30 x 30 x 30 mm 60
Figure 5.2 3D model of the lattice specimen type 20 x 20 x 20 mm 60
Figure 5.3. Example of a card for a material class 62
Figure 5.4. Pairs of points of true stress - true strain for the first 5 defect classes (failure at the first element) 63
Figure 5.5. Example card with curve parameters for a material class 64
Figure 5.6. Example of linking a material card to a part card for a class 65
Figure 5.7. Creation of the part set containing all part cards 65
Figure 5.8. Extract of the 'element_beam.k' file with random association of a PID to each element 67
Figure 5.9. Association of a different material card to each beam segment: different colors correspond to different MID (30 x 30 mm cell) 68
Figure 5.10. Association of a different material card to each beam segment: different colors correspond to different MID (20 x 20 mm cell) 68
Figure 5.11. Visualization of properties for a material card in LS-DYNA 69
Figure 5.12. Quasi-static case: card for the fixed upper Rigid wall 70

Figure 5.13. Quasi-static case: card for the lower rigid wall with linear displacement.. 70
Figure 5.14. Definition of linear displacement for the lower rigid wall: Assigning an LCSS value of 1 71
Figure 5.15. 3D model of the test specimen for the quasi-static compression case with the presence of the two RIGID WALLS, fixed and movable (30 x 30 mm cell) 71
Figure 6.1. Representative flow chart of the steps performed for the creation of the finite element model with a multiscale approach..... 72
Figure 6.2 Experimental curves obtained from quasi-static compression tests on specimens with respectively 20x20 mm and 30x30 mm cells 73
Figure 6.3.Compression of the test specimen in 3 successive simulation frames with reference to axial beam stress 75
Figure 6.4 Force-displacement curve for a defect-free case on a 20x20 mm cell, unfiltered 76
Figure 6.5 Force-displacement curve for case without defects (20x20 mm cell), with a cosine filter at 108 Hz..... 77
Figure 6.6 Comparison between the experimental curve and the numerical curve for a nominal beam diameter of d=1.31 mm. Above: on a 20 x 20 mm cell. Below: on a 30 x 30 mm cell..... 78
Figure 6.7 Numerical force-displacement comparison curves between the diameter d=1.31 mm and the minimum diameter achieving the same mass as the real specimen. The upper graph corresponds to the 20 x 20 mm cell, while the lower graph corresponds to the 30 x 30 mm cell 80
Figure 6.8 Determination of the effective beam diameter d=1.2 mm and the corresponding Force-Displacement curve obtained (red curve). The upper graph corresponds to the 20 x 20 mm cell, while the lower graph corresponds to the 30 x 30 mm cell..... 82
Figure 6.9 Determination of the FAIL parameter achieving the best approximation (blue curve) of the experimental curve. The upper graph corresponds to the 20 x 20 mm cell, while the lower graph corresponds to the 30 x 30 mm cell 83
Figure 6.10 Numerical test curves with internal defects and comparison with the experimental curve. Case with a 20 x 20 mm cell 85
Figure 6.11 Numerical test curves with internal defects and comparison with the experimental curve. Case with a 30 x 30 mm cell 85
Figure 6.12 Determining the band of numerical curves and comparison with the experimental curve. The upper graph corresponds to the 20 x 20 mm cell, while the lower graph corresponds to the 30 x 30 mm cell 87
Figure 6.13 Comparison between the experimental curve and the design numerical curve. The upper graph corresponds to the 20 x 20 mm cell, while the lower graph corresponds to the 30 x 30 mm cell 88

List of Tables

Table 3.1 Mechanical properties of the Alluminium alloy AlSi10Mg..... 9
Table 3.2 Discretization of the distribution into defect classes for the two cell types..... 25
Table 4.1 Pairs of values extrapolated from the stress-strain curve of the AlSi10Mg specimen..... 28
Table 4.2 Defect classes with their respective volume fraction and variable RVE side length..... 40
Table 4.3 Defect classes with the imposition of a maximum limit on the RVE side equal to the beam diameter..... 50

1 Introduction

1.1 Lattice structure

Additive Manufacturing technologies, increasingly evolving in recent years, enable the creation of intricate geometries and complex shapes that are not reproducible using traditional mechanical processing techniques. An advanced example of what is achievable is lattice or reticular structures, which are obtained by repeating a basic cell of varying geometry until it completely fills a portion of the component (Figure 1.1 [1]).

In particular, selective laser melting (SLM) has enabled the development of lattice structures with unique properties. By controlling various parameters, lattice structures allow the realization of unique mechanical, electrical, thermal, and acoustic properties and have received significant research attention.

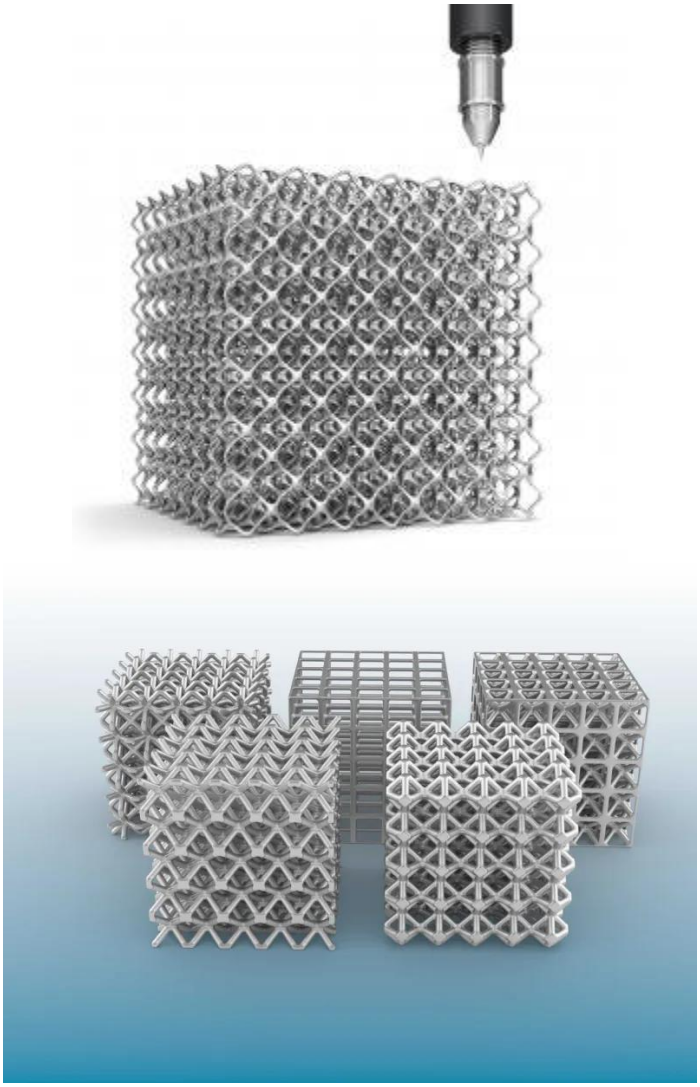

Figure 1.1. Example of lattice structures produced with AM technologies [1]

Lattice structures are a type of cellular material that is characterized by the regular repetitive structure of their unit cells. While the unit cells of lattice structures can be analyzed like space frames using classical mechanics, a lattice structure should be considered as a material with its own mechanical properties, allowing for a direct comparison between the properties of a lattice structure and those of its parent structure.

Lattice structures can generally be categorised based on their mechanical response as being either bending-dominated or stretch-dominated. Bending-

dominated structures experience bending moments within their structure and so are compliant, whereas stretch-dominated structures experience axial loads, meaning they are stiffer and stronger than bending-dominated structures.
Characterized by their porous nature and composed of a network of repetitive geometric structures, these structures can take on various cell topology such as cubic cells, hexagonal patterns, or more complex structures. The choice of configuration depends on the specific application needs and the functional requirements of the final object.
A lattice structure's cell topology defines whether it will be bending or stretch-dominated.

The lattice specimens analyzed in this thesis exhibit an octet cell type structure (the third in Figure 1.2), belonging to the "stretch-dominated" category, which provides the best compromise between absorbed energy and total mass [2].
As shown in Figure 1.2, the basic 'octlet' unit cell comprising the lattice specimens includes beams oriented at 0° and 45°, while there are no beams oriented vertically. This cell will be uniformly repeated throughout the lattice specimen.

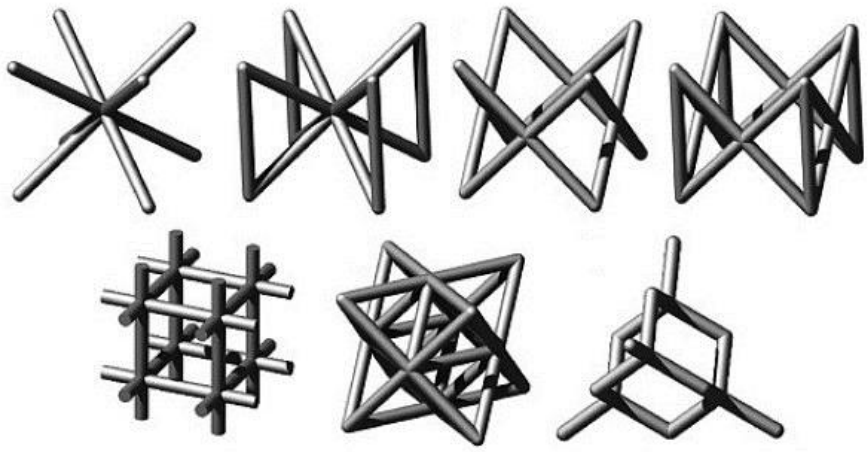

Figure 1.2. Examples of unit cell configurations for lattice structures. The octlet cell is the second from the bottom [3]

The utilization of lattice structures in additive manufacturing offers several advantages. Firstly, these structures are lightweight due to their high porosity: this allows for a significant reduction in the overall weight of the object, which can be advantageous in sectors like aerospace and automotive where weight is a critical factor.

Furthermore, lattice structures exhibit high strength and impact energy absorption capacity despite their lightweight nature. The distribution of forces through the lattice framework enables excellent mechanical strength, ensuring the ability to withstand significant loads.

Finally, lattice structures also offer a wide design freedom. Additive Manufacturing enables the creation of complex shapes, allowing for the fabrication of lattice components optimized for specific requirements.

However, designing lattice structures requires specialized expertise to ensure structural integrity and production process efficiency. Additionally, the presence of internal and surface defects that occur as a result of the Active

Manufacturing process can complicate post-printing processing, such as surface finishing or coatings application.

Despite these challenges, the potential offered by this type of component allows for pushing the boundaries of performance and design possibilities in the realm of 3D printing.

1.2 Multiscale method

Finite Element Analysis (FEA) used to study the structural behavior of mechanical components can, however, lead to large-scale models with high computational costs when analyzing complex structures such as the lattice structures under examination. The use of a multiscale approach in FEA analysis allows for a simpler solution to this problem. This method involves integrating different resolution scales into a single analysis, enabling greater computational efficiency without compromising the accuracy of the results.

The multiscale method divides the complex model into various regions or levels of detail, each of which is analyzed with an appropriate resolution. The information obtained from each level of detail is then combined to provide a global solution [4].

It is possible to link different analysis scales, as many heterogeneous mechanical components are difficult to analyze directly with finite element computational techniques. Therefore, a localized analysis step is performed, introducing the concept of the 'Representative Volume Element' (RVE). Once the representative micro volume with the same properties as the starting component is identified and defined, localized boundary conditions (μBCs) compatible with the multiscale method are applied.

By obtaining mechanical properties at the microscopic or local level, these can then be transferred to the global model using homogenization techniques, allowing for an accurate representation of the overall behavior of the component.

Figure 1.3 depicts the functional diagram of the multiscale design approach method. [5].

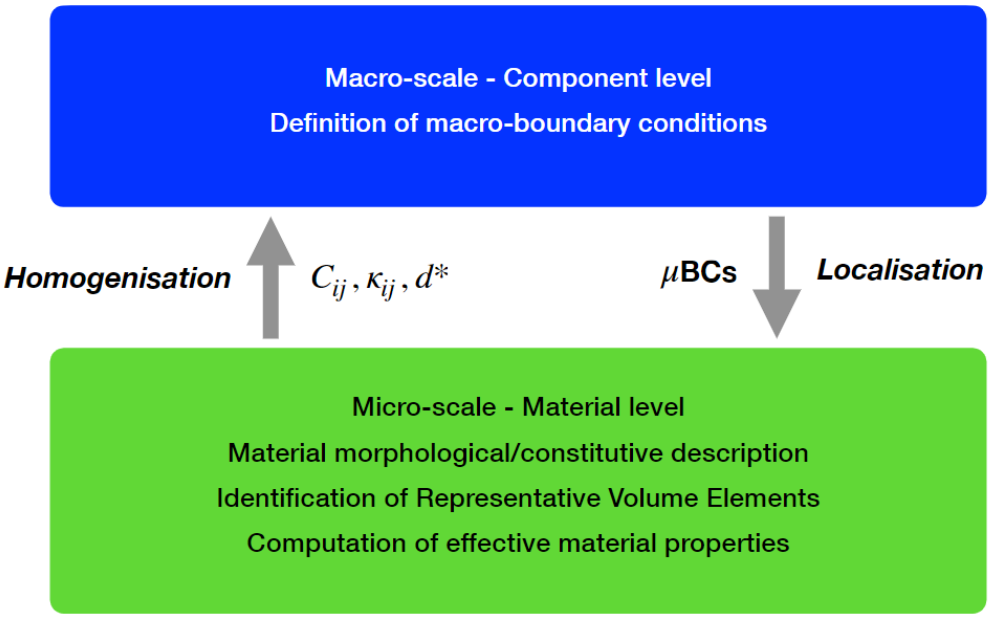

Figure 1.3. Multiscale approach: homogenization and localization techniques [5]

The use of the multiscale method in FEA for complex components offers several advantages. Firstly, it substantially reduces computational complexity, enabling the analysis of components that would otherwise demand impractical computation times. Additionally, it provides an accurate representation of the component's behavior at various scales, allowing for a more comprehensive assessment of structural performance.

2 Thesis objective

As previously mentioned, the aim of this thesis is to simulate the mechanical behavior of lattice structure components produced through Additive Manufacturing.
In particular, the aim is to study the behavior of the lattice structure under quasi-static compressive load and numerically estimate its response in terms of Force - Displacement.

In the subsequent chapters, the methods adopted for conducting multiscale Finite Element Analysis (FEA) on lattice specimens will be explained. This will involve creating mechanical strength curves, which are then extrapolated to the macro-scale of the specimen using homogenization techniques.

A crucial aspect of the research is focused on characterizing internal defects within the material. Scans performed on lattice specimens revealed the presence of internal porosity within the beams of the structure, thereby reducing the effective material volume.

The multiscale approach has enabled the consideration of defects on a local scale, which are then extended to the macroscopic scale of the specimen. This approach accounts for the defectiveness on both local and larger scales, ensuring a comprehensive understanding of the material's behavior.

Once the stress-strain behavior has been simulated for each microscale element, including defects, a force-displacement response was obtained for the lattice specimen (macroscale) and compared with the actual response. The variability introduced by the defects will then allow to create a band bounded by two lower and upper curves that encompass the experimental response.

The final step involved establishing the numerical design curve corresponding to a defect-free material model. This curve will be used for future Finite Element Analysis (FEA) without the need to repeat the study with defects.

3 Experimental analysis

3.1 Material characteristics

The lattice structure specimens under examination were produced using Additive Manufacturing through the Selective Laser Melting (SLM) technique, Using aluminum alloy AlSi10Mg powder.

The SLM (Selective Laser Melting) process is an Additive Manufacturing (AM) technology used for selectively melting metal powders to create parts. This is achieved by employing a high-power concentrated laser beam on a bed of metal powders.

The aluminum alloy AlSi10Mg, used in the powder bed, exhibits the mechanical properties listed in table 3.1.

AlSi10Mg	
Density	2,9 g/cm^3
Elastic Modulus	69000 MPa
Poisson ratio	0,33

Table 3.1 Mechanical properties of the Alluminium alloy AlSi10Mg

Tensile tests conducted on AlSi10Mg specimens produced using SLM techniques have generated results in terms of the Stress-Strain curve, following a tensile test, as shown in Figure 3.1.

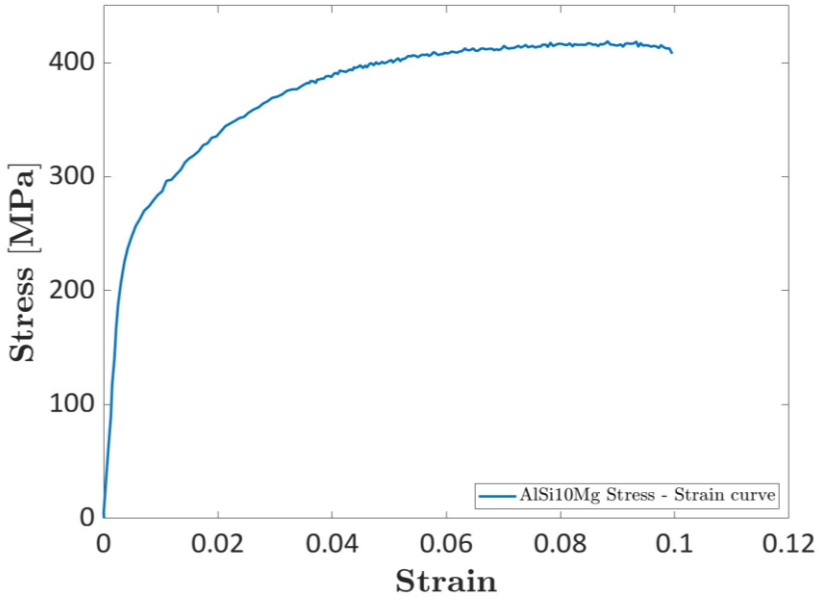

Figure 3.1. Experimental engineering stress-strain curve of the AlSi10Mg lattice specimen

3.2 Experimental tests

For the purpose of comparison with experimental data obtained on pure material, compression and nano-indentation tests were conducted in the laboratory on specimens created using the SLM technique.

Since the production process is the same for creating the final lattice structure, these analyses are used to assess the influence of the manufacturing process on the mechanical properties of the Additive Manufacturing component.

3.2.1 Specimens geometry

To perform the compression tests, two specimens made of AlSi10Mg As Built were prepared by cutting from a rectangular 4 mm thick cross-section bar, produced via SLM (Selective Laser Melting).
The specimens have dimensions of 100 x 8 x 4 mm and were fabricated by cutting from the bar using water jet cutting.
Once designed in CAD, the specimens were saved in .dxf format so that the files could also be read by the software connected to the waterjet cutting machine in use.

Nano-indentation tests, on the other hand, necessary for determining Vickers hardness and elastic modulus values, were conducted directly on the lattice structure with the octlet-type cell, as previously introduced.

3.2.2 Compression test

Since the lattice structure is subjected to a compressive load, the material's behavior was determined through a compression test.
Compression tests were conducted on the two specimens, and a free inflection length was calculated at which to clamp the two ends of the beam to avoid buckling phenomena.
In the compression test, the specimen is gripped at both ends, creating a clamped-guided (CG) configuration as shown in Figure 3.2. This results in a maximum free span for avoiding buckling, which is $L_{eff} = 0.5\ L_0$ where $L_0 = 100$ mm.
For safety reasons, a free deflection length of 15 mm was still considered.

The test was carried out at the DIMEAS laboratory of the Polytechnic University of Turin, and the machine used for the test is an Instron 8801, as shown in Figure 3.3.

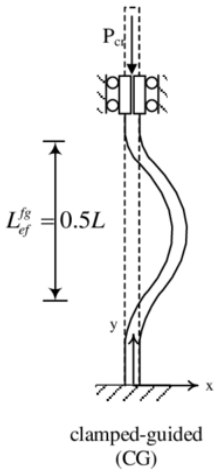

Figure 3.2 Clamped-guided (CG) configuration of the specimen during the compression test

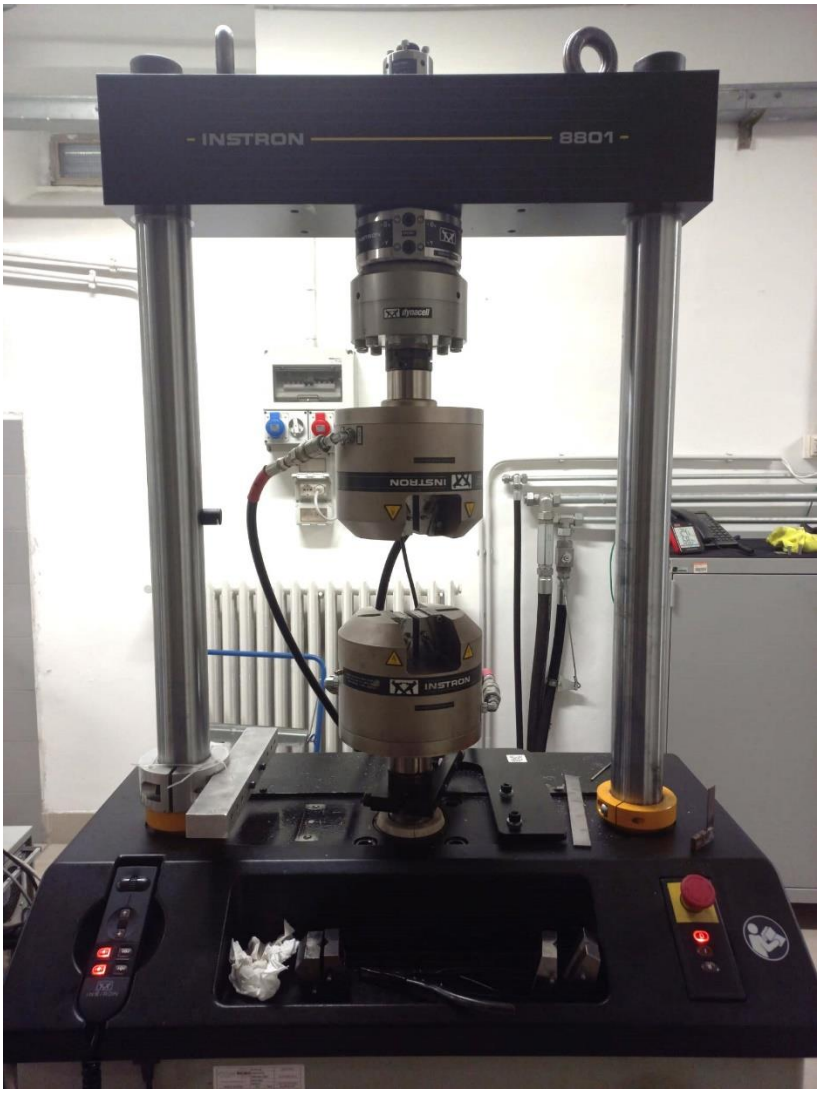

Figure 3.3 The machine used for the compression test: Instron 8801

Due to the inability to install strain gauges within the specimen due to limited space, two arbitrary points were monitored using an optical microscope. By acquiring their position before and after the test, it was possible to determine through the Digital Image Correlation (DIC) technique (Figure 3.4).

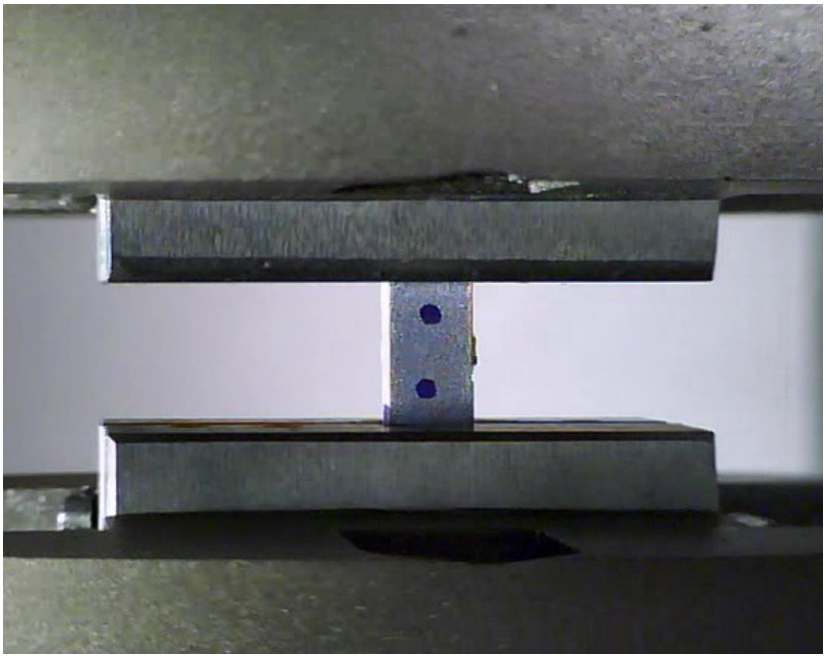

Figure 3.4 Image of the specimen in the machine acquired by the optical microscope

Unfortunately, the specimen still experienced buckling: this is due to the fact that AM techniques generally produce a geometry that is not perfectly flat and may have some surface defects. The test was therefore interrupted as soon as this phenomenon appeared.

Figure 3.5 shows the specimen subjected to the compression test, where it can be observed that the structure has indeed undergone buckling.

Figure 3.5 Image of the specimen undergoing a compression test, with the occurrence of buckling

The Force-Displacement data obtained from the compression test were then used to determine the Stress-Strain curve for comparison with the reference curve previously obtained from an AlSi10Mg alloy produced through Selective Laser Melting (Figure 3.1). In Figure 3.6, the comparison is shown: the blue curve obtained from the new compression test was prematurely interrupted due to the specimen undergoing buckling. However, this phenomenon occurred in the plastic deformation range, beyond the yield point, so the result is still acceptable for the purpose of comparison.

Although there is a slight variability at the yield point, the curve obtained from the new compression test tends to approximate the red curve again, before the test interruption due to buckling.

Consequently, it can still be concluded that from the new compression tests performed, the specimens produced using SLM exhibit behavior that approximates the actual behavior of the AlSi10Mg alloy produced through Additive Manufacturing.

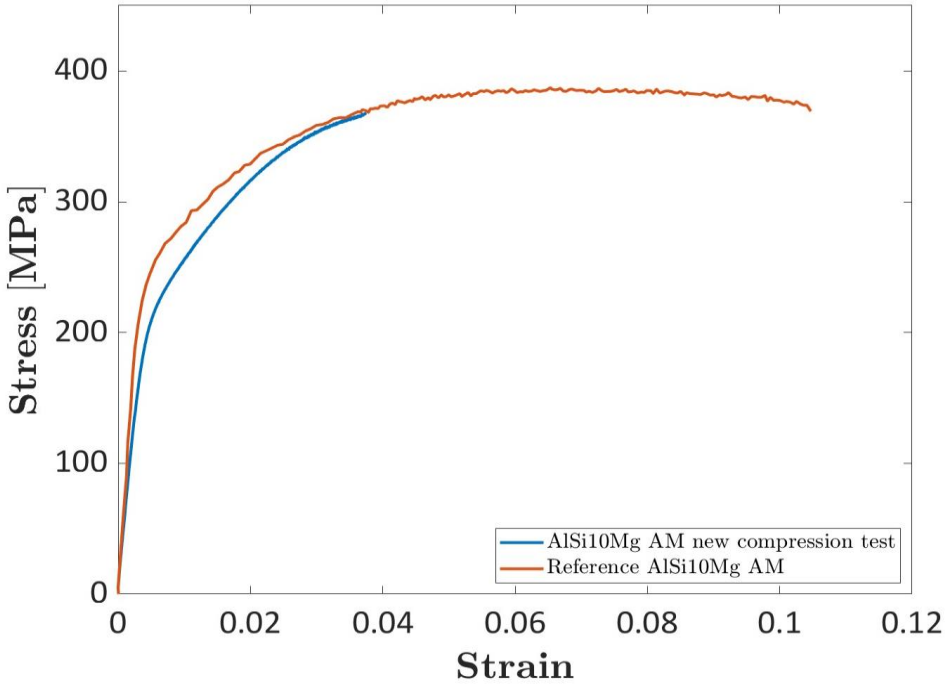

Figure 3.6 Comparison of stress-strain curves between the reference AlSi10Mg alloy (red curve) and that obtained from the quasi-static compression test on a new AlSi10Mg specimen (blue curve)

3.2.3 Nano – indentation test

The nanoindentation tests are microhardness tests conducted to determine the elastic modulus and Vickers hardness values for the AlSi10Mg alloy produced using AM.

During the nanoindentation, a very hard tip is pressed into the sample, and the variation of load versus the penetration depth is recorded: in this way, it is possible to determine the hardness of the material.

The tests were performed directly on the lattice structure beams using a diamond indenter. Indentations were made at the 45° oriented beams and at

some nodes of the structure.

An important aspect is the depth of indentation in the tests: in the study *Review of Nanoindentation Size Effect: Experiments and Atomistic Simulation* [6], the influence of dimensional effects on resulting hardness was analyzed. In particular, the nanoindentation tests conducted demonstrate what was stated in the study: the depth of indentation experimentally influences hardness and the elastic modulus. Therefore, tests were conducted by increasing the depth of indentation until achieving a convergence of hardness and the elastic modulus.

In order to determine the elastic modulus, a convergence study was conducted due to the high variability in values obtained depending on the test locations. In Figure 3.7, the elastic modulus values obtained at various indentation depths are reported.

There is a noticeable convergence to a value of approximately 53 GPa for measurements conducted on the 45° oriented beams and 45° oriented nodes. Therefore, this value was considered as the elastic modulus for the lattice, adopted in the subsequent design phase.

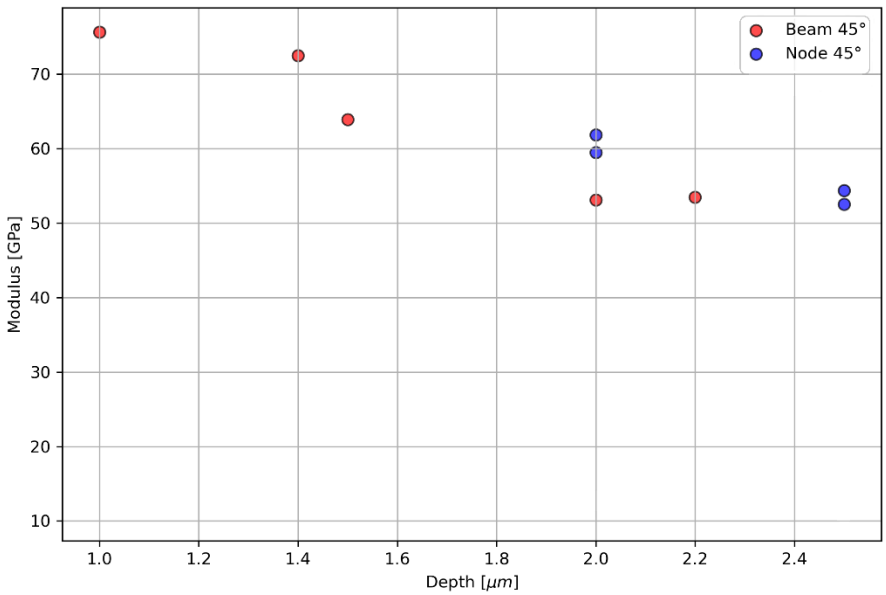

Figure 3.7 Elastic modulus values as a function of penetration depth, for various measurements

3.3 Internal defects

In Figure 3.8, the lattice specimen under examination is shown, which was created using Additive Manufacturing techniques starting from AlSi10Mg powders: the typical compact beam-shaped structure is observed.

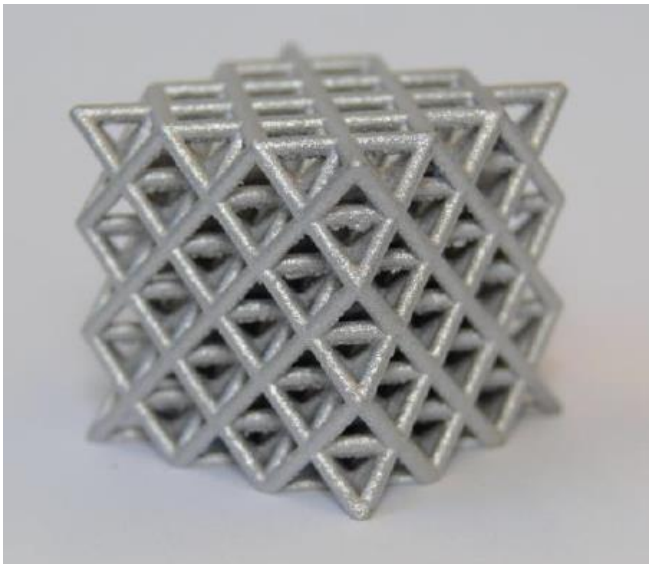

Figure 3.8 Lattice structure specimen made of AlSi10Mg aluminum alloy undergoing compression testing

Scanning electron microscopy (FESEM) images (Figure 3.9) of one of the lattice cell faces reveal the presence of high surface roughness, which is typical of additive manufacturing parts. However, the effect of surface roughness on mechanical behavior will not be considered in this study. The diameters of the structure's beams are also not exactly constant, with some variations related to the manufacturing process. In the initial approximation for the subsequent creation of the finite element model, a nominal diameter $d_{beam} = 1{,}31\,mm$ was specified.

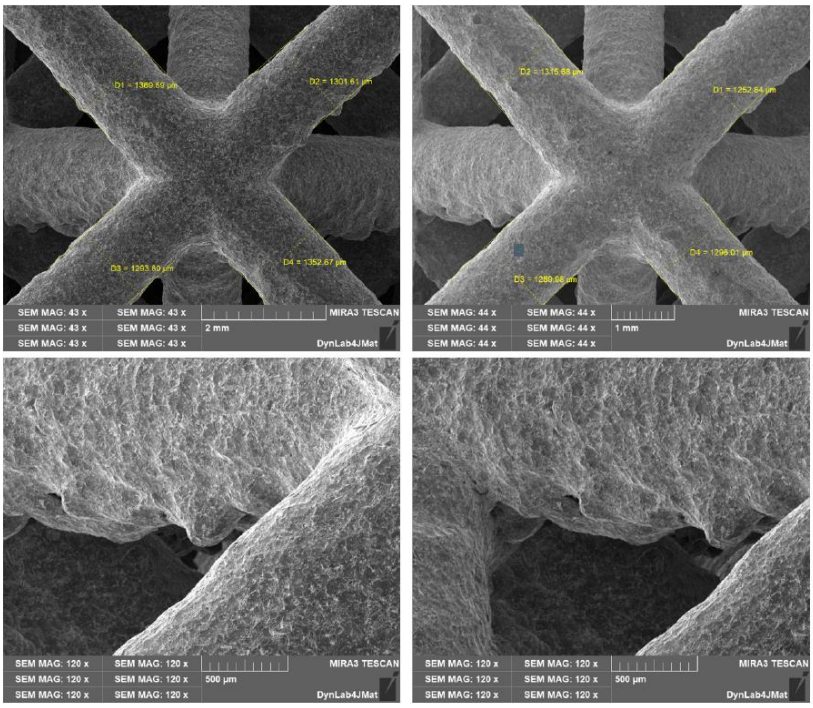

Figure 3.9 Images of the specimen surface captured by the scanning electron microscope

Micro-computed tomography scans were also conducted on the specimen, revealing the presence of internal defects (structural porosity) that decrease the effective material volume and, consequently, mechanical strength.

By performing Micro-CT scans at various points within the structure, the porosities highlighted by the scans within the structure exhibit a geometry that can be approximated as a sphere.

In Figure 3.10, the three-dimensional reconstruction of the specimen based on the grayscale after a Micro-CT scan has been presented.

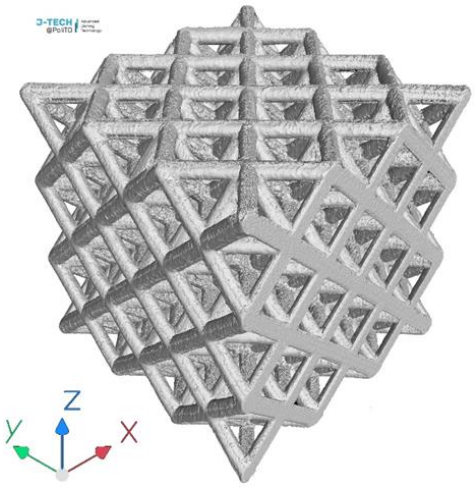

Figure 3.10 Three-dimensional reconstruction of a specimen based on the grayscale

Furthermore, in Figure 3.11, the view on the xy plane of a scan is shown, highlighting the presence of a defect at a node of the structure.

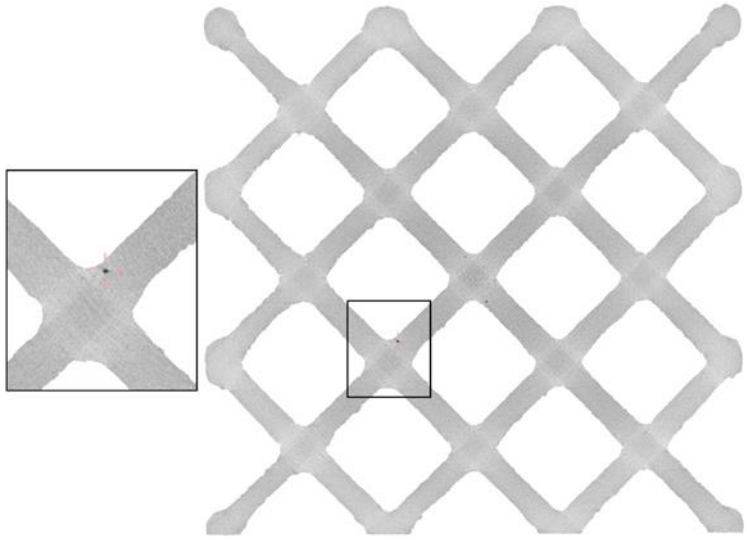

Figure 3.11 View on the XY plane of a scan, with a focus on an internal spherical defect at the intersection of two structural beams

The data for all possible internal defects, characterized by different sphere diameters, were collected and reported in an Excel document.

For each defect size, analyzing how many times it repeats within the porous structure resulted in the determination of a distribution for each defect class. Two different defect distributions have been determined for the specimens with cell sizes of 20 x 20 x 20 mm and 30 x 30 x 30 mm, as shown in Figure 3.12 and Figure 3.13.

These are expressed in terms of probability as a function of the equivalent spherical defect size. It can be observed that for the 20 x 20 mm cell, defects tend to cluster at lower nominal values of equivalent defect diameter.

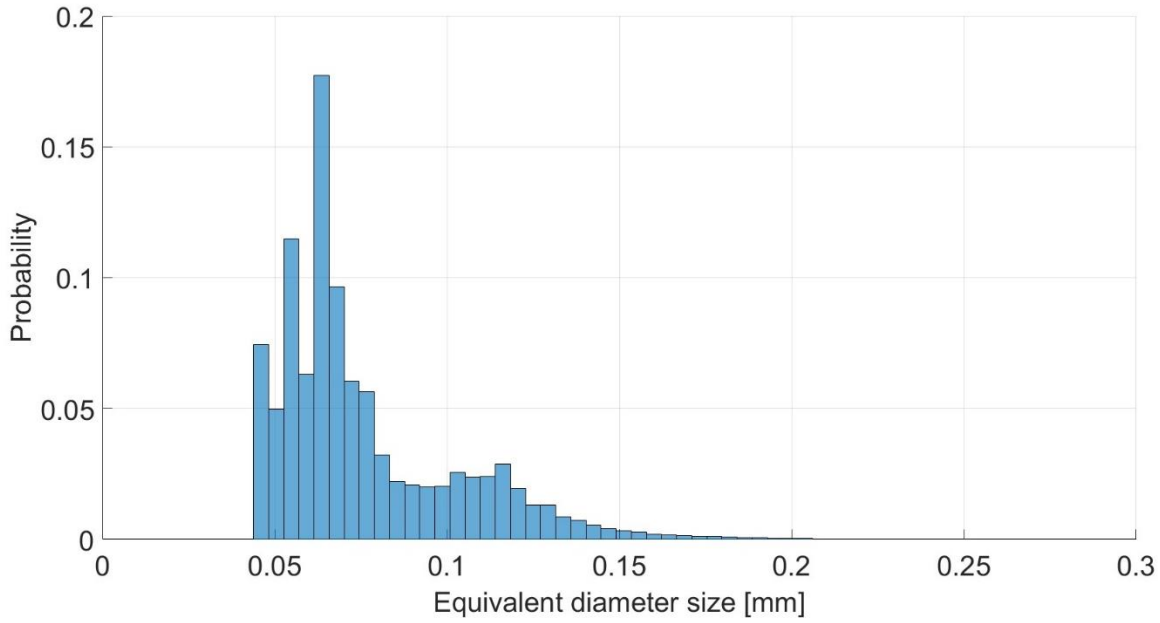

Figure 3.12 Probability distribution of the defects in the 20 x 20 x 20 mm specimen for each size

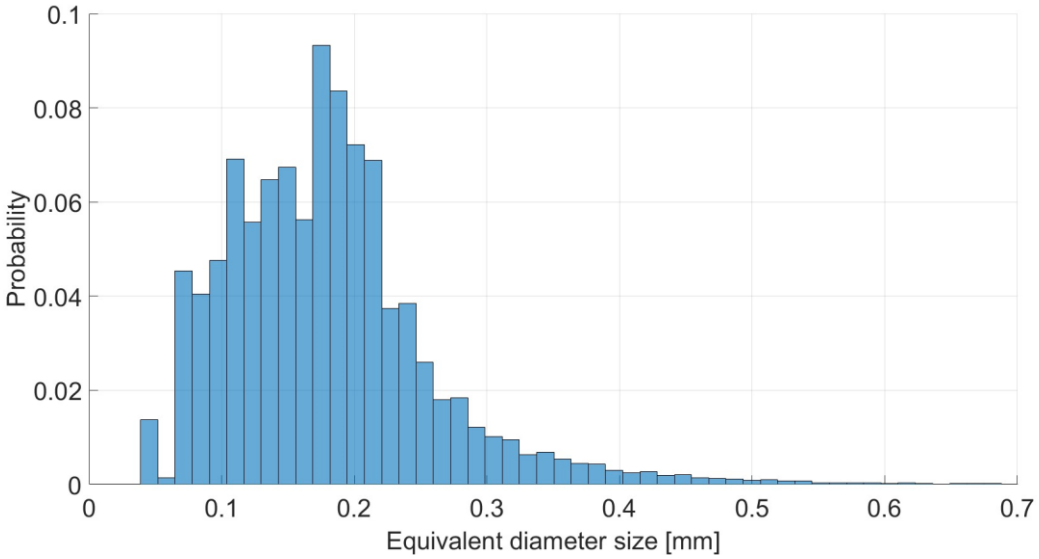

Figure 3.13. Probability distribution of the defects in the 30 x 30 x 30 mm specimen for each size

This defect distribution has been discretized into defect classes and utilized in the multiscale analyses on the component.

Previous research on these specimens simulated mechanical behavior without employing a multiscale approach. It involved dividing the lattice specimen using 1D beam elements. The presence of defects was simplified by performing localized reductions in the beam diameter (notches) distributed randomly across the various beams of the structure.

However, the analysis conducted in this study approached the problem differently, using a multiscale approach with 3D elements at the local level (microscale) and considering defects as spherical voids within the local three-dimensional domain.

The previous distributions were discretized into probability intervals, resulting in a series of defect classes, reported in Table 3.2. Defects with diameters greater

than 0.532 mm were neglected due to their low probability of occurrence in the structure.

30x30 mm Cell			20x20 mm Cell		
ID	Defect diameter [mm]	Probability	ID	Defect diameter [mm]	Probability
1	0.038	0.0137	1	0.048	0.0745
2	0.052	0.0142	2	0.052	0.0497
3	0.065	0.0453	3	0.057	0.115
4	0.091	0.0477	4	0.061	0.0631
5	0.104	0.069	5	0.066	0.177
6	0.117	0.056	6	0.07	0.0967
7	0.13	0.065	7	0.075	0..605
8	0.143	0.067	8	0.078	0.0565
9	0.156	0.056	9	0.0833	0.0322
10	0.169	0.093	10	0.088	0.0221
11	0.182	0.084	11	0.092	0.0208
12	0.195	0.072	12	0.096	0.0199
13	0.208	0.069	13	0.1	0.0204
14	0.221	0.037	14	0.105	0.0256
15	0.234	0.039	15	0.109	0.0239
16	0.247	0.026	16	0.114	0.0239
17	0.26	0.018	17	0.118	0.0288
18	0.27	0.018	18	0.123	0.0196
19	0.286	0.012	19	0.127	0.013
20	0.299	0.01	20	0.132	0.0131
21	0.312	0.009	21	0.136	0.0086

22	0.325	0.006	22	0.14	0.00737
23	0.338	0.007	23	0.145	0.00531
24	0.351	0.005	24	0.149	0.00403
25	0.363	0.0045	25	0.154	0.00326
26	0.376	0.004	26	0.158	0.00286
27	0.389	0.003	27	0.162	0.00197
28	0.402	0.0024	28	0.167	0.00186
29	0.415	0.00277	29	0.171	0.00137
30	0.428	0.00191	30	0.175	0.00125
31	0.441	0.00204	31	0.18	0.00112
32	0.454	0.00139	32	0.184	0.00097
33	0.467	0.00123	33	0.189	0.00068
34	0.48	0.00118	34	0.193	0.0006
35	0.493	0.00092	35	0.197	0.00044
36	0.506	0.00102	36	0.206	0.00028
37	0.519	0.00073	37	0.223	0.00024
38	0.532	0.00071	38	0.237	0.00012

Table 3.2 Discretization of the distribution into defect classes for the two cell types

Once all this information about the experimental specimen was obtained, it was possible to use it as input for creating the numerical model using a multiscale approach to the problem.

4 Representation of the model using a multiscale method

According to the application of a previously introduced multiscale method for the numerical resolution of the problem, it is necessary to divide the problem into a micro and macro scale. The problem was indeed addressed by starting with an analysis at the microscale: to do this, the representative local structure model was defined.

An RVE (Representative Volume Element) is a fundamental portion of the initial model that exhibits the same mechanical properties as the base structure on a macroscale.

Two types of elements have been selected to create the RVE:

1. Cubic Representative Volume Element: Initially, a three-dimensional cubic element representing the material was defined as the starting point at the local scale.
2. Cylindrical representative element beams of the structure.

FEA simulations to determine the Stress-Strain behavior were performed using Abaqus CAE software. Initially, it was necessary to define the elastic and plastic properties of the material as input.

As seen in the previous chapter, the lattice structure specimen exhibits a reduced elastic modulus compared to the nominal value of 53 GPa, which is typical for an AlSi10Mg aluminum alloy. Consequently, the original stress-strain curve in Figure 3.1 was modified to accommodate the reduced elastic

modulus from 69 GPa to 53 GPa.

A new yield strain has been calculated at the same stress level, after which an offset of the curve was performed to determine the new stress-strain points in the plastic deformation range.

Although the reduction is not particularly significant, the decrease in the slope of the elastic region results in an increase in plastic deformation at failure (Figure 4.1).

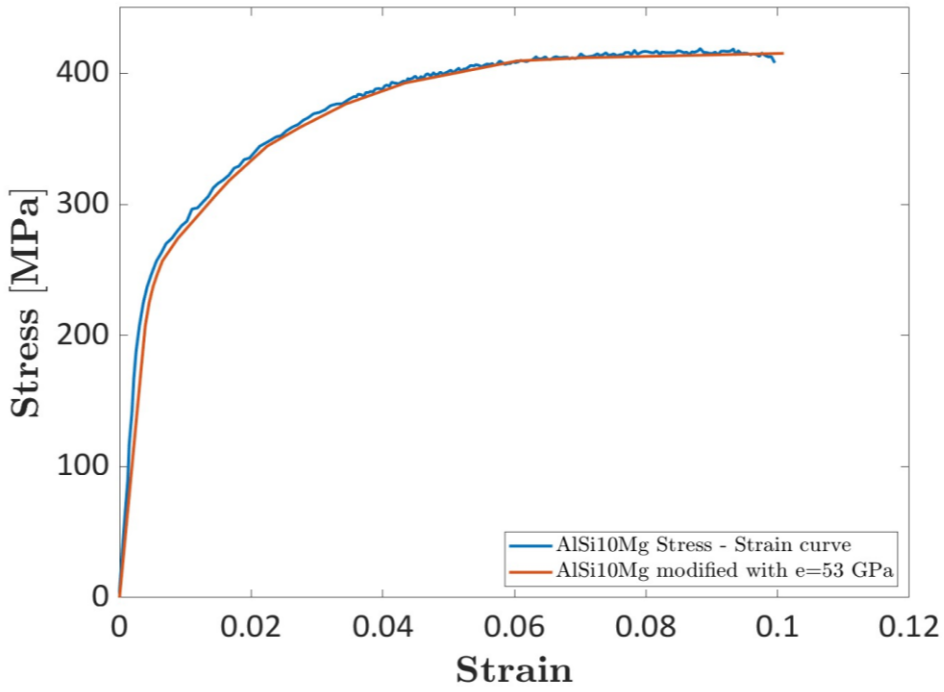

Figure 4.1 Comparison between the nominal curve of AlSi10Mg and the curve of AlSi10Mg manufactured through Additive Manufacturing (AM) for lattice structure. The new elastic modulus determined from nanoindentation tests is 53000 MPa

The new plastic region was discretized into 15 points and incorporated as a reference plastic property in Abaqus.

Plastic Strain	Stress [Mpa]
0	207.1989
0.000602	225.0659
0.001184	237.0891
0.001782	246.0445
0.002608	256.8235
0.004945	273.9836
0.007263	287.1251
0.010564	306.1181
0.012796	318.3537
0.018513	344.3244
0.023584	358.9237
0.030506	376.5842
0.039538	392.616
0.056436	409.362
0.066353	411.7897
0.097022	415.1682

Table 4.1 Pairs of values extrapolated from the stress-strain curve of the AlSi10Mg specimen

For both the cubic RVE and the cylindrical beam cases, a Python script was created to automatically generate the model in Abaqus, inserting the appropriate boundary and loading conditions, and launching the FEA analysis.

Internal defects within the element were treated as spherical cavities within the cube. The script allows for the generation of one or more internal spherical defects, divided by defect class.

A crucial aspect was how to consider the presence of defects within the element to conduct FEA simulations subsequently. The choice of considering all defect classes randomly inserted within the element until a certain volume fraction (the ratio of the volume subtracted by the defects to the volume of the model) is reached is actually incorrect.

The volume fraction cannot be uniquely determined for all defect classes because, for small-sized RVEs, the VF results in less defect filling. Furthermore, this approach does not properly account for the presence of large defects in small RVEs, as such a defect would immediately exceed the volume fraction and not be considered in the automatic generation of defects.

The better choice is to perform simulations separately for each defect class. In other words, one spherical defect of different sizes should be inserted into the element one at a time. Subsequently, the material response curves at the local scale can be used as equivalent properties on the specimen.

4.1 Multiscale analysis with cubic RVE

4.1.1 Model geometry

Initially, a cubic-shaped RVE was considered, inside which spherical cavities were created. As can be seen from Figutre 4.2, the spherical defect is generated with the center sphere coordinates (x, y, z) randomly positioned within the element.

Any generation that results in an intersection with a face or edge of the cube leads to the creation of a cavity representing the complementary portions of the sphere on opposite faces. This situation, besides being possible in a real case, is necessary when periodic boundary conditions are applied to the RVE.

These boundary conditions are the most commonly used in a multiscale approach and will be explained in more detail in the following paragraph.

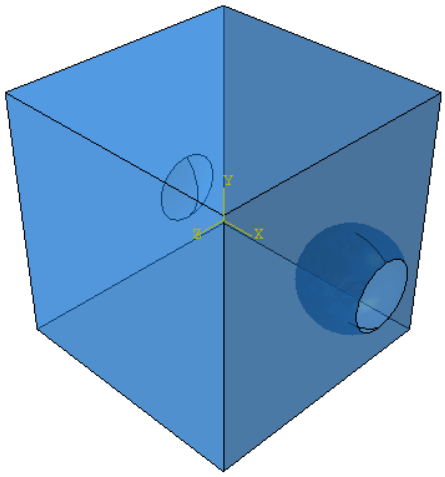

Figure 4.2 RVE model with internal spherical defect created in Abaqus CAE

4.1.2 Boundary conditions

An important aspect of multiscale simulations is the boundary conditions, which also play a crucial role in computational homogenization.

The choice of boundary conditions influences the result of homogenization, including the constitutive response at the macro-scale, the size of the RVE, and the type (and extent) of localized failure that occurs at the micro-scale.

As detailed in the report *BEMs for Multiscale Materials Modelling* [5], it has been demonstrated how the most accurate approximations for mechanical properties at the RVE level can be achieved when periodic boundary conditions are adopted, rather than uniform traction or linear displacement boundary conditions.

In the context of FEA analysis with the multiscale method, periodic boundary conditions are applied on opposite edges of the analysis domain to account for the periodic repetition. Thus, it's necessary for geometric continuity to be ensured between opposite faces of the RVE. After generating the mesh, the nodes on two opposite faces within the cube must be equal in number.

Between each pair of nodes across the two faces, equations are defined in terms of displacement. The constraint on this displacement is imposed by defining a set of 3 dummy nodes, called dummy nodes, at the origin of the coordinate system.

As explained in the study *Applying Periodic Boundary Conditions in Finite Element Analysis* [7], multiple points may be constrained by a general linear combination of nodal variables (such as displacements at different nodes). The summation of the product of a coefficient and the corresponding nodal variable is equal to a

fixed displacement $\hat{u}$ applied to the dummy node. Specifically, we define a general linear homogeneous equation:

$$A_1 u_i^P + A_2 u_j^Q + \cdots + A_N u_k^R = \hat{u} \tag{4.1}$$

Where R is node, k is degree of freedom, i.e. 1, 2, or 3 which represent x, y, z directions, A_N is a constant coefficient that define the relative motion of nodes.

In the case of a cubic RVE, the general equations for multi-node periodic systems are modified to take on the form for each coordinated direction:

$$u_1^{left} - u_1^{right} = \hat{u}_x \tag{4.2}$$

$$u_2^{left} - u_2^{right} = \hat{u}_y \tag{4.3}$$

$$u_3^{left} - u_3^{right} = \hat{u}_z \tag{4.4}$$

Where $\hat{u}_x$, $\hat{u}_y$, $\hat{u}_z$ are the displacements set on the 3 dummy nodes of the element.

After the creation of the RVE element, the solid mesh of TETRA elements is automatically generated through a Python script. The element size changes based on the RVE's dimensions, but in general, it's defined to be 1/10 of the cube's side length (Figure 4.3).

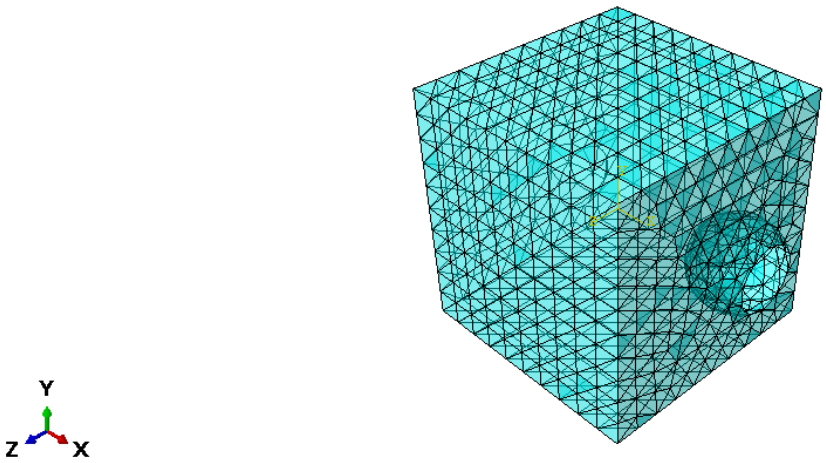

Figure 4.3 RVE model with 3D Tetra mesh

At last, an input file named "job.inp" containing information about the number of nodes and elements in the structure is automatically generated. This file is imported into MATLAB, where, through an implemented function, an additional import file is created containing data for applying periodic boundary conditions (PBC). The function counts nodes on each face and establishes pairs of nearest nodes between opposite faces, generating periodicity equations between the two nodes and the corresponding dummy node.

This process results in a "PBC.inp" file, which is added to the same working directory as the ongoing simulation. By running a second Python script in Abaqus, a new import to the model from the "job.inp" file is performed, using an INCLUDE statement for the "PBC.inp" file.

This sequence creates a new RVE model with the added periodic boundary conditions. In Figure 4.4, yellow circles represent all nodes on the involved faces in the periodic boundary condition equations.

Three highlighted red circles are representing three nodes that constitute one of the equations for periodic boundary conditions (4.2). The central node serves as

the dummy node to which the prescribed displacement is applied, while the two outer circles represent the two nodes on opposite faces connected by the displacement equation.

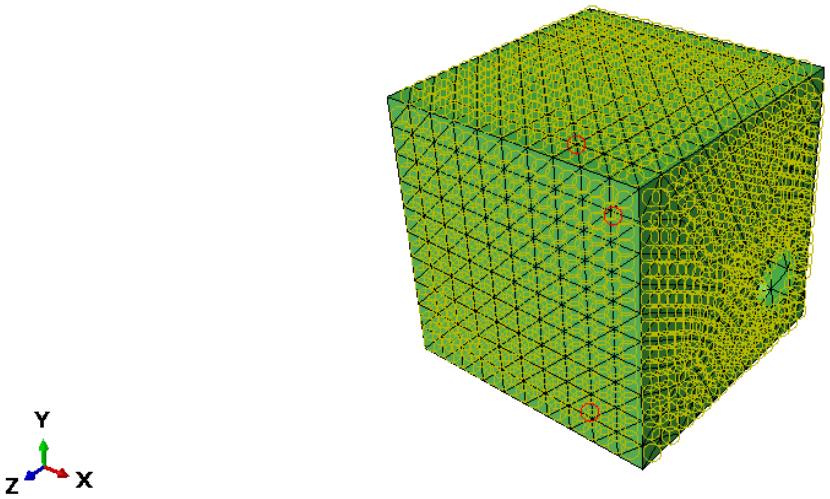

Figure 4.4 Periodic boundary conditions on the RVE and focus on the nodes of a single equation

4.1.3 Definition of the displacement and constraint

Subsequently, the script automatically defines the displacements for the RVE. By imposing displacements on the dummy nodes in the three coordinate directions, it is possible to simulate normal tensile or compressive stresses. Additionally, by combining pairs of displacements between two dummy nodes, resulting shear stresses can also be obtained.

To prevent rigid body motions, in the RVE simulations, a constraint is defined on one of the structure's nodes. In this case, a vertex node of the element was chosen.

The Python generation script creates a step containing the displacement $\hat{u}_x$, which is imposed on the element (Figure 4.5).

The aim is to study the behavior of lattice material under compression. To achieve this, a step corresponding to compression along the x-axis of the RVE (σ_{xx}) was analyzed, setting a known displacement $\hat{u}_x$.

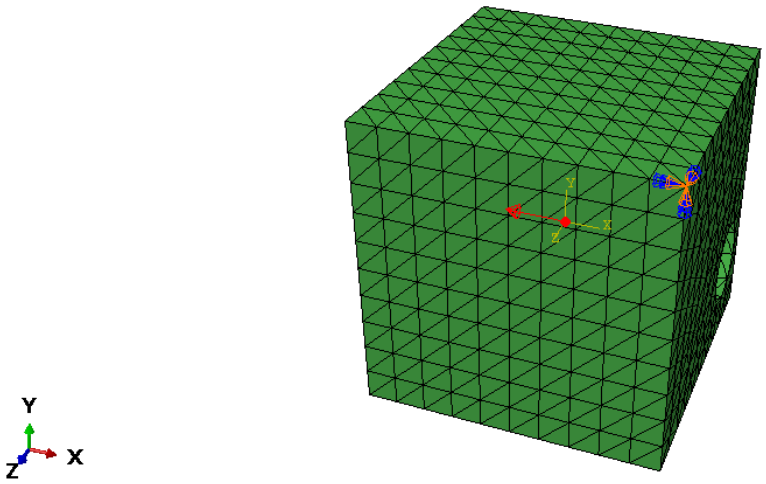

Figure 4.5 Imposition of a fixed constraint on a vertex and displacement at the dummy node

Finite element simulations are conducted by imposing a displacement and simulating the mechanical behavior under compression until reaching the specified strain value.

A displacement of 0.104 mm was chosen for the RVE, imposed on the dummy nodes. This value corresponds to the ultimate strain of the real material, obtained from the experimental curve (Figure 4.6).

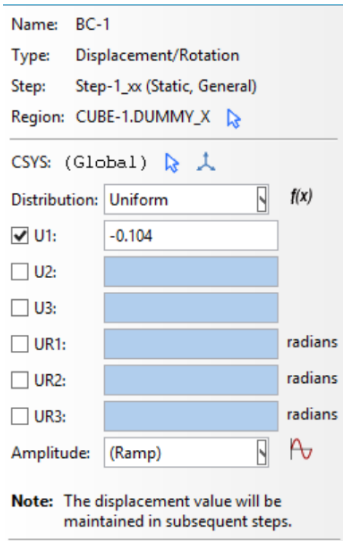

Figure 4.6. Parametrization of the displacement at the dummy node

It was chosen to adopt a subdivision of 35 equally spaced intervals for the Field Output frames of the simulation. This choice was made to adequately represent both the elastic and plastic fields with a sufficient number of points. In cases where frames are calculated automatically, the solver tended not to execute calculations during the initial phase for stresses below the yield limit. As a result, there were no insights into the elastic zone, which is necessary for a potential assessment of convergence to the real elastic modulus value of 53000 MPa, involving a sensitivity study.

4.1.4 FE simulations on the RVE

Once all the parameters for the RVE are defined, the script automatically allows to create a Job in Abaqus and execute the FEA simulation on the RVE element.

Since only one displacement u_x hat is imposed at the dummy-x node for the study at hand, it results in deformation along the x-axis of the RVE. Through this analysis, it is possible to visualize the stress σ_{11} and strain ε_{11} behavior for a compression loading along the x-axis.

Given that the size of the RVE at the local scale is arbitrary, two possible approaches were evaluated:

1. Considering a fixed RVE size equal to the diameter of the beam that constitutes the specimen (1,31 mm).
2. Calculating the individual sides of the RVE while taking into account the probability of defects appearing in the model. This approach calculates a volume of defects for each defect class within the specimen and determines the RVE size, which will vary for each defect class. In this latter case, the volume fraction of each defect is used to change the size of the RVE based on the volume fraction of each defect class.

The volume of the ideal specimen is known to be $V_{ideal\ specimen} = 8750\ mm^3$, while the volume of the real specimen, obtained from scans, is $V_{real\ specimen} = 6500\ mm^3$. Therefore, the total volume of defects in the specimen is $V_{tot\ difects} = 2250\ mm^3$.

The volume occupied by defects belonging to a given class $V_{tot,class}$ is calculated as follows:

$$V_{tot,class} = p_{class} \cdot V_{tot\ defects} \tag{5.1}$$

Dove p_{class} represents the probability of each defect class.
So, the volume fraction of each defect class $vol\ frac_{class}$ will be:

$$vol\ frac_{class} = \frac{V_{tot,class}}{V_{ideal\ specimen}} \tag{5.2}$$

Also, the volume of each individual defect $V_{single\ defect}$ is known and calculable as the volume of a sphere:

$$V_{single\ defect} = \frac{4}{3}\pi \cdot d_{defect}^3 \tag{5.3}$$

It becomes possible to determine the RVE's volume $V_{RVE,class}$ for each defect class, and consequently its side length $l_{RVE,class}$.

This approach assumes that we maintain the volume fraction of each defect class both at the macroscopic level of the specimen and at the microscopic level of the RVE. This ensures the calculation of equivalent properties.

$$V_{RVE,class} = \frac{V_{single\ defect}}{vol\ frac_{class}} \rightarrow\ l_{RVE,class} = \sqrt[3]{V_{RVE,class}} \tag{5.4}$$

In Table 4.2, the results obtained using this method are presented, where the respective side length to assign to the RVE can be observed for various defect classes.

d_{CLASSE} [mm]	Defect volume (sphere) [mm^3]	Probability	V_{CLASS} in specimen [mm^3]	Vol_frac classe	V_{RVE} [mm^3]	Side $_{RVE}$ [mm]
0.038	2.87309E-05	0.0137	30.825	0.0035229	0.0082	0.2013
0.052	7.36222E-05	0.0142	31.95	0.0036514	0.0202	0.2722
0.065	0.000143793	0.0453	101.925	0.0116486	0.0123	0.2311
0.091	0.000394569	0.0477	107.325	0.0122657	0.0322	0.3180
0.104	0.000588977	0.069	155.25	0.0177429	0.0332	0.3214
0.117	0.000838603	0.056	126	0.0144000	0.0582	0.3876

0.13	0.001150347	0.065	146.25	0.0167143	0.0688	0.4098
0.143	0.001531111	0.067	150.75	0.0172286	0.0889	0.4463
0.156	0.001987799	0.056	126	0.0144000	0.1380	0.5168
0.169	0.002527311	0.093	209.25	0.0239143	0.1057	0.4728
0.182	0.003156551	0.084	189	0.0216000	0.1461	0.5267
0.195	0.003882419	0.072	162	0.0185143	0.2097	0.5941
0.208	0.004711819	0.069	155.25	0.0177429	0.2656	0.6428
0.221	0.005651652	0.037	83.25	0.0095143	0.5940	0.8406
0.234	0.006708821	0.039	87.75	0.0100286	0.6690	0.8746
0.247	0.007890227	0.026	58.5	0.0066857	1.1802	1.0568
0.26	0.009202772	0.018	40.5	0.0046286	1.9883	1.2574
0.27	0.010305995	0.018	40.5	0.0046286	2.2266	1.3058
0.286	0.01224889	0.012	27	0.0030857	3.9695	1.5834
0.299	0.013996266	0.01	22.5	0.0025714	5.4430	1.7591
0.312	0.01590239	0.009	20.25	0.0023143	6.8714	1.9011
0.325	0.017974164	0.006	13.5	0.0015429	11.6499	2.2669
0.338	0.02021849	0.007	15.75	0.0018000	11.2325	2.2395
0.351	0.02264227	0.005	11.25	0.0012857	17.6107	2.6017
0.363	0.025044854	0.0045	10.125	0.0011571	21.6437	2.7868
0.376	0.027833137	0.004	9	0.0010286	27.0600	3.0022
0.389	0.03082105	0.003	6.75	0.0007714	39.9532	3.4186
0.402	0.034015494	0.0024	5.4	0.0006171	55.1177	3.8057
0.415	0.037423372	0.00277	6.2325	0.0007123	52.5398	3.7454
0.428	0.041051585	0.00191	4.2975	0.0004911	83.5838	4.3723
0.441	0.044907036	0.00204	4.59	0.0005246	85.6071	4.4073
0.454	0.048996627	0.00139	3.1275	0.0003574	137.0809	5.1562
0.467	0.053327259	0.00123	2.7675	0.0003163	168.6047	5.5245

0.48	0.057905836	0.00118	2.655	0.0003034	190.8384	5.7573
0.493	0.062739258	0.00092	2.07	0.0002366	265.2022	6.4248
0.506	0.067834429	0.00102	2.295	0.0002623	258.6280	6.3713
0.519	0.07319825	0.00073	1.6425	0.0001877	389.9450	7.3058
0.532	0.078837623	0.00071	1.5975	0.0001826	431.8180	7.5585

Table 4.2 Defect classes with their respective volume fraction and variable RVE side length

The FE analyses were performed on a number of RVEs equal to the number of defect classes shown in Table 4.2.

Depending on the loading conditions, what matters to know is the axial deformation (E11) and axial stress (S11), both oriented along the x axis.

As an example, it is reported the analysis of the case corresponding to the defect class with d_{defect} = 0.169 mm, which is the one that has the highest probability of occurring in the structure and therefore a higher volume fraction. In this approach, this is the most critical class, as it has the smallest l_{RVE}/d_{defect} ratio.

In Figure 4.7, the contour plot on the Representative Volume Element (RVE) is shown with results in terms of strain E11 along the x axis.

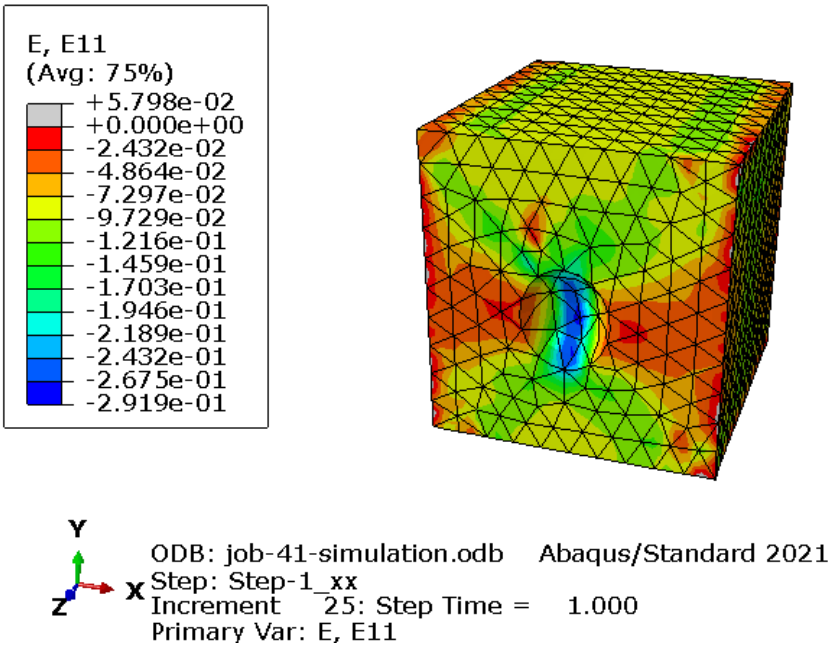

Figure 4.7. Finite Element Analysis (FEA) results: deformation induced on the RVE

What needs to be determined in order to establish the Stress-Strain curves of the RVE are the stress and strain values for each simulation output frame. For this purpose, a Python function named 'Data_extraction_odb' was created. Once executed within Abaqus CAE, it reads the output .odb file of the FEA simulation. For the specified stress and strain component, it calculates the integral average over all elements. Since the elements are 3D Tetrahedral, the FE model evaluates stress characteristics at integration points of each element, which often coincide with individual nodes. An average stress and strain value is calculated for each mesh element, and then an integral average is taken over all elements to obtain a unique value for the entire RVE.

Given that there is compression along the x-axis, the directional stress and strain values S11 and E11 are the ones that need to be collected. The function also calculates the elastic modulus E for each output frame, useful for analyzing the convergence of the method in the elastic field.

Not all parts of the model will fail at the same time, but some more stressed elements will reach the value of ultimate strain sooner. In generating the response curves, this additional variability has been taken into account by counting the elements that exceed the real ultimate strain value at each response frame. The writing of the text file containing stress-strain point pairs stops at the frame where at least 10% of the mesh elements locally exceed the ultimate strain value.

The choice was made to consider a certain number of elements relative to the total (in this case, 10%) rather than stopping when the first element exceeds that value. This is because based on the geometry of the cubic RVE and the presence of internal cavities, it was seen that Abaqus can generate distorted elements that develop stress concentrations and excessively high strain values.

In this case, as evident in Figure 4.8, focusing on two Tetrahedral elements, there are high compression and tensile stress values developing at the connecting node. These high values distort the contour plot of the model. This is a mesh error and should not be considered in the result analysis.

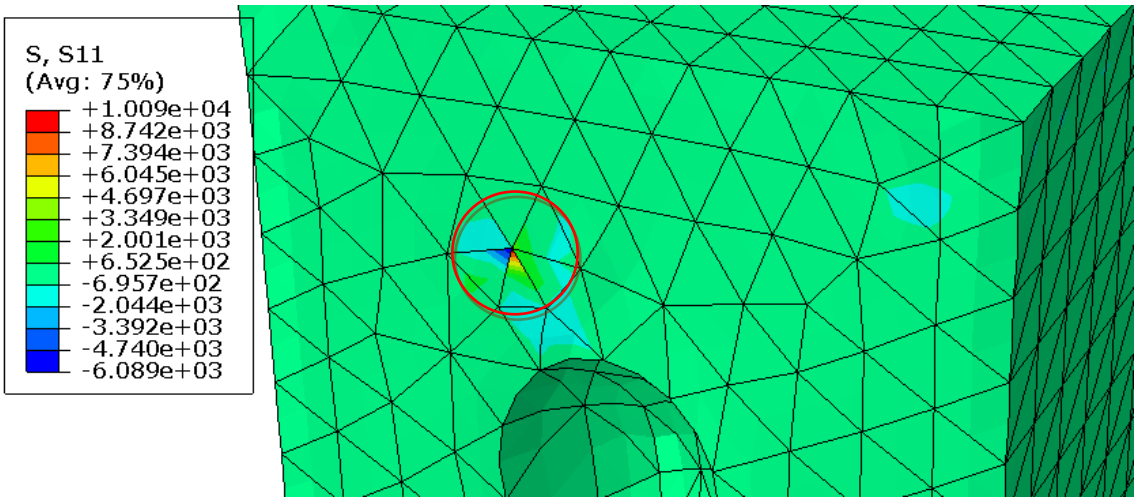

Figure 4.8. Stress concentration between two elements due to mesh errors

By setting upper and lower labels for the visualization scale a more detailed view of stress distribution can be seen (Figure 4.9).

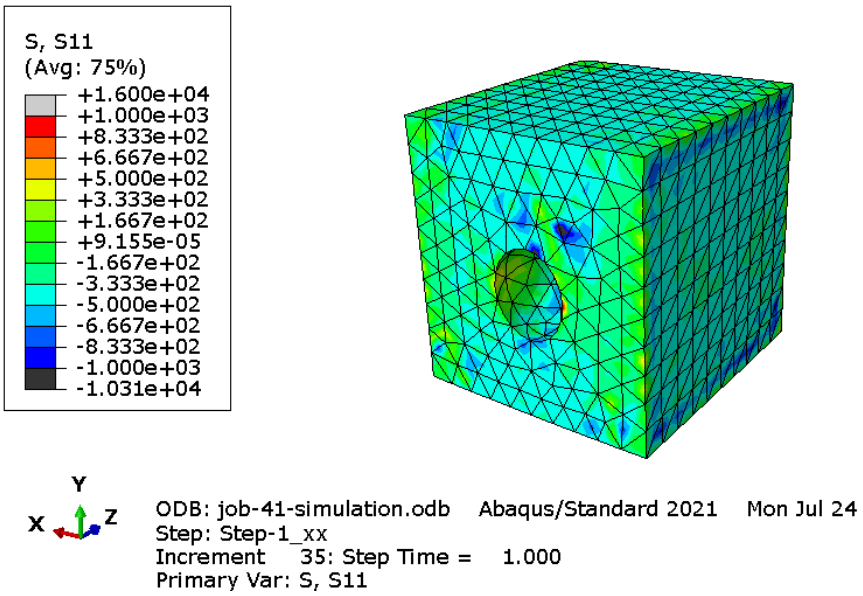

Figure 4.9. Stress distribution after setting a minimum and maximum value in the contour plot

4.1.5 Analysis of the results

Once all the finite element simulations for the defect classes constituting the defect distribution were performed, the .odb output files were analyzed to extract the stress values S11 and strain values E11 on the RVE.

The Python function reads the odb file of the model and generates the following text file containing the averaged stress and strain values over the RVE, the elastic modulus E, as well as the volume of the RVE as the sum of the volumes of individual mesh elements.

In Figure 4.10 is an excerpt from the file for the first 8 simulation frames, displaying the total volume of the RVE.

Stress	Strain	Elastic Modulus	Max Element Strain
-141.843463842	-0.00268387131817	52850.3221752	-0.00561745511368
-222.315910511	-0.00524812683746	42361.0018196	-0.0147989848629
-249.500598512	-0.00783688402214	31836.7093104	-0.0233986154199
-267.247290931	-0.010452862	25566.9012879	-0.0314747206867
-281.952185377	-0.0130802943548	21555.4923864	-0.0390989482403
-295.22861186	-0.0157066287248	18796.4341064	-0.0467064976692
-307.15637703	-0.0183270291054	16759.7473254	-0.0545835979283
-317.749731999	-0.0209432270255	15171.9566241	-0.0627300813794
-327.034224904	-0.0235530211124	13885.0223648	-0.0711823999882
-335.13959365	-0.0261561223147	12813.0458184	-0.0799849629402
-342.19710589	-0.028757637264	11899.3470412	-0.0889906138182
-348.457624292	-0.0313543483442	11113.5342526	-0.0981971547008

Total Model Volume: 1.08211636427

Figure 4.10. Stress and strain data, elastic modulus value obtained from the ODB file

In each frame, a counter keeps track of the number of elements that have exceeded the imposed strain (equal to the material's ultimate strain) and displays this count on the screen. The Figure 4.11 shows an excerpt of the counting process. In this case, 1912 represents 10% of the total elements in the model.

```
Elements at failure: 1905
Elements at failure: 1906
Elements at failure: 1907
Elements at failure: 1908
Elements at failure: 1909
Elements at failure: 1910
Elements at failure: 1911
Elements at failure: 1912
Max n. elements reached
```

Figure 4.11. Count of elements at failure in the model

The data obtained from the FEA simulations for each defect class are compiled into an Excel spreadsheet used as a data collection base. A Matlab script was then created to generate stress-strain plots based on the data from each class.

As a result, families of curves are obtained for the two examined cases (fixed RVE with side equal to the beam's diameter and variable RVE based on the

volume fraction of each defect class). These curves shift downwards progressively compared to the experimental curve as the defect influences the mechanical strength.

Different analysis approaches yield different results. For each approach, the obtained curves for defect classes are shown. Concerning the initial convergence of the method in the elastic range, it is observed that it is respected. Even with variations in the RVE size, it does not affect the mechanical behavior in the elastic range.

In fact, by focusing on the elastic range (up to the maximum yield stress), it can be noticed that the elastic modulus achieved at the first simulation frame, representing the yield point, deviates slightly from the actual value (Figure 4.12).

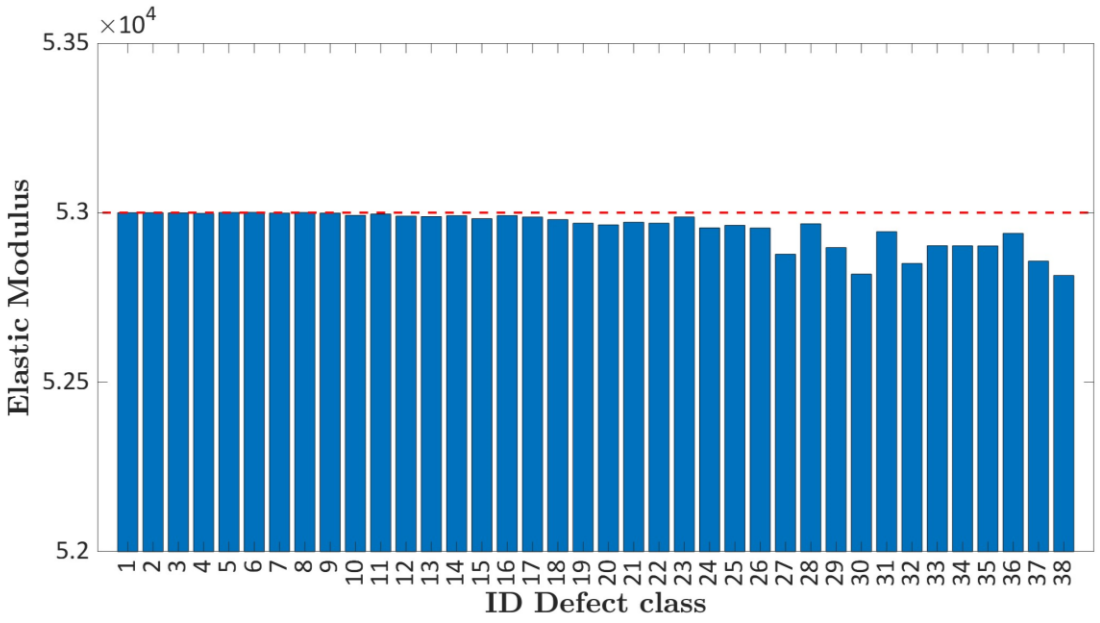

Figure 4.12. Convergence of the elastic modulus for FEA simulations

Case with fixed RVE

The simulations conducted on fixed-side RVEs with a diameter equal to the beam's diameter (1.31 mm) led to material responses in terms of stress-strain curves, as shown in Figure 4.13. Only specific defect classes were analyzed to establish an initial range. What can be observed is that for larger defects within the material (defect class diameter greater than approximately 0.3-0.4 mm), there is a variability in the curves compared to the experimental ones.

For smaller defects, however, the influence of the defect is very minimal, meaning that the defect diameter is too small to impact the RVE size. In reality, this approach does not account for the probability of defect classes occurring within the section: defect classes with diameters smaller than 0.3 mm have the highest likelihood, so the volume fraction of defects must be taken into consideration.

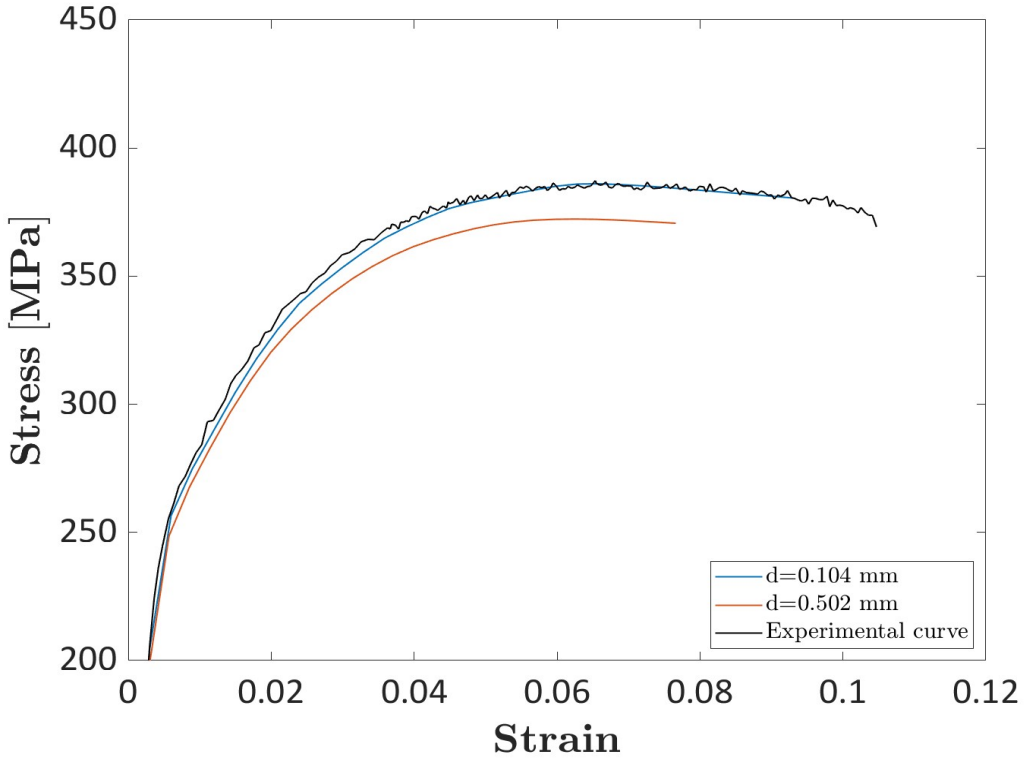

Figure 4.13. Trend of curves with internal defects for fixed-side RVEs with a side length of 1.31 mm. The green curve represents the experimental data of the specimen

Case with variable RVE

In the previously analyzed case, the volume fraction of each defect class, which is linked to the probability of occurrence in the specimen, was not considered. By following the approach described earlier, with RVEs varying based on the volume fraction occupied by each defect class, new stress-strain curves were obtained.

In Figure 4.14 the results obtained by considering the failure of the RVEs when at least 10% of the mesh elements exceed the specified ultimate strain value are reported. Globally, the curves stop before reaching the failure strain indicated by the experimental curve.

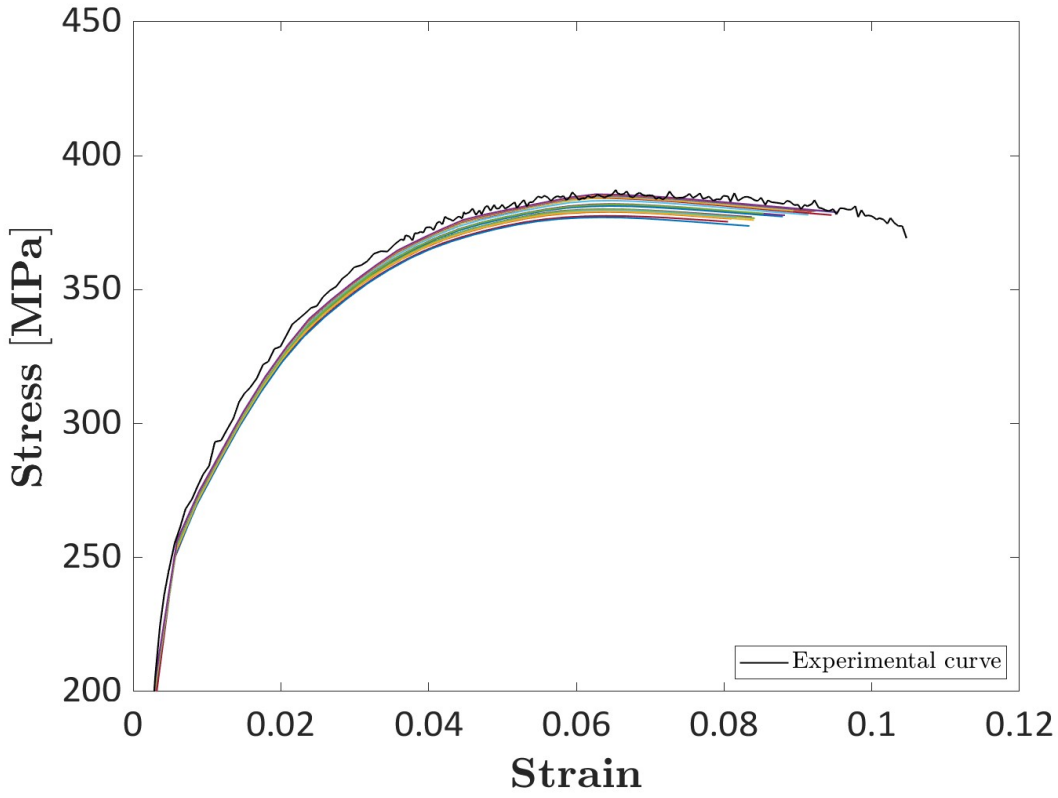

Figure 4.14. Stress-strain curve variabile RVE: reduction of the ultimate strain for each curve when at least 10% of the elements reach failure

Following this approach, however, larger defects, which according to the distribution from Micro-CT scans (shown in Figure 3.13 and Figure 3.14) have a lower probability of occurring in the sample, will also result in a larger volume fraction and therefore larger RVE dimensions, reducing the influence of the defect. The beams have a diameter of 1.31 mm, and considering larger RVEs for estimating mechanical properties would diminish the effect of larger defects.

As a result, it was ultimately decided to set an upper limit of 1.31 mm for the RVE dimensions to accurately account for the potential impact of larger defects

within the beam. Although less likely, the presence of larger defects was indeed demonstrated by the Micro-CT scans of the sample.

The new distribution for defect classes is presented in Table 4.3, considering the volume fraction occupied by defects and imposing an upper limit on the resulting RVE dimensions, determined by the 1.31 mm diameter of the beams.

Using this limit on the size of the Representative Volume Element (RVE), new stress-strain curves have been determined, as shown in Figure 4.15.

d_{class} [mm]	Vol_{defect} (sphere) [mm^3]	Probability	$Vol_{defect\ class}$ [mm^3]	Vol-fraction defect class	Vol_{RVE} [mm^3]	Side RVE [mm]
0.038	2.87309E-05	0.0137	30.825	0.0035229	0.0082	0.2013
0.052	7.36222E-05	0.0142	31.95	0.0036514	0.0202	0.2722
0.065	0.000143793	0.0453	101.925	0.0116486	0.0123	0.2311
0.091	0.000394569	0.0477	107.325	0.0122657	0.0322	0.3180
0.104	0.000588977	0.069	155.25	0.0177429	0.0332	0.3214
0.117	0.000838603	0.056	126	0.0144000	0.0582	0.3876
0.13	0.001150347	0.065	146.25	0.0167143	0.0688	0.4098
0.143	0.001531111	0.067	150.75	0.0172286	0.0889	0.4463
0.156	0.001987799	0.056	126	0.0144000	0.1380	0.5168
0.169	0.002527311	0.093	209.25	0.0239143	0.1057	0.4728
0.182	0.003156551	0.084	189	0.0216000	0.1461	0.5267
0.195	0.003882419	0.072	162	0.0185143	0.2097	0.5941
0.208	0.004711819	0.069	155.25	0.0177429	0.2656	0.6428
0.221	0.005651652	0.037	83.25	0.0095143	0.5940	0.8406
0.234	0.006708821	0.039	87.75	0.0100286	0.6690	0.8746
0.247	0.007890227	0.026	58.5	0.0066857	1.1802	1.0568
0.26	0.009202772	0.018	40.5	0.0046286	1.9883	1.2574
0.27	0.010305995	0.018	40.5	0.0046286	2.2266	1.3058
0.286	0.01224889	0.012	27	0.00545	3.9695	1.3100
0.299	0.013996266	0.01	22.5	0.00623	5.4430	1.3100
0.312	0.01590239	0.009	20.25	0.00707	6.8714	1.3100
0.325	0.017974164	0.006	13.5	0.008	11.6499	1.3100
0.338	0.02021849	0.007	15.75	0.00899	11.2325	1.3100

0.351	0.02264227	0.005	11.25	0.01007	17.6107	1.3100
0.363	0.025044854	0.0045	10.125	0.01114	21.6437	1.3100
0.376	0.027833137	0.004	9	0.01238	27.0600	1.3100
0.389	0.03082105	0.003	6.75	0.01371	39.9532	1.3100
0.402	0.034015494	0.0024	5.4	0.01513	55.1177	1.3100
0.415	0.037423372	0.00277	6.2325	0.01665	52.5398	1.3100
0.428	0.041051585	0.00191	4.2975	0.01826	83.5838	1.3100
0.441	0.044907036	0.00204	4.59	0.01998	85.6071	1.3100
0.454	0.048996627	0.00139	3.1275	0.02179	137.0809	1.3100
0.467	0.053327259	0.00123	2.7675	0.02372	168.6047	1.3100
0.48	0.057905836	0.00118	2.655	0.02576	190.8384	1.3100
0.493	0.062739258	0.00092	2.07	0.02791	265.2022	1.3100
0.506	0.067834429	0.00102	2.295	0.03017	258.6280	1.3100
0.519	0.07319825	0.00073	1.6425	0.03256	389.9450	1.3100
0.532	0.078837623	0.00071	1.5975	0.03507	431.8180	1.3100

Table 4.3 Defect classes with the imposition of a maximum limit on the RVE side equal to the beam diameter

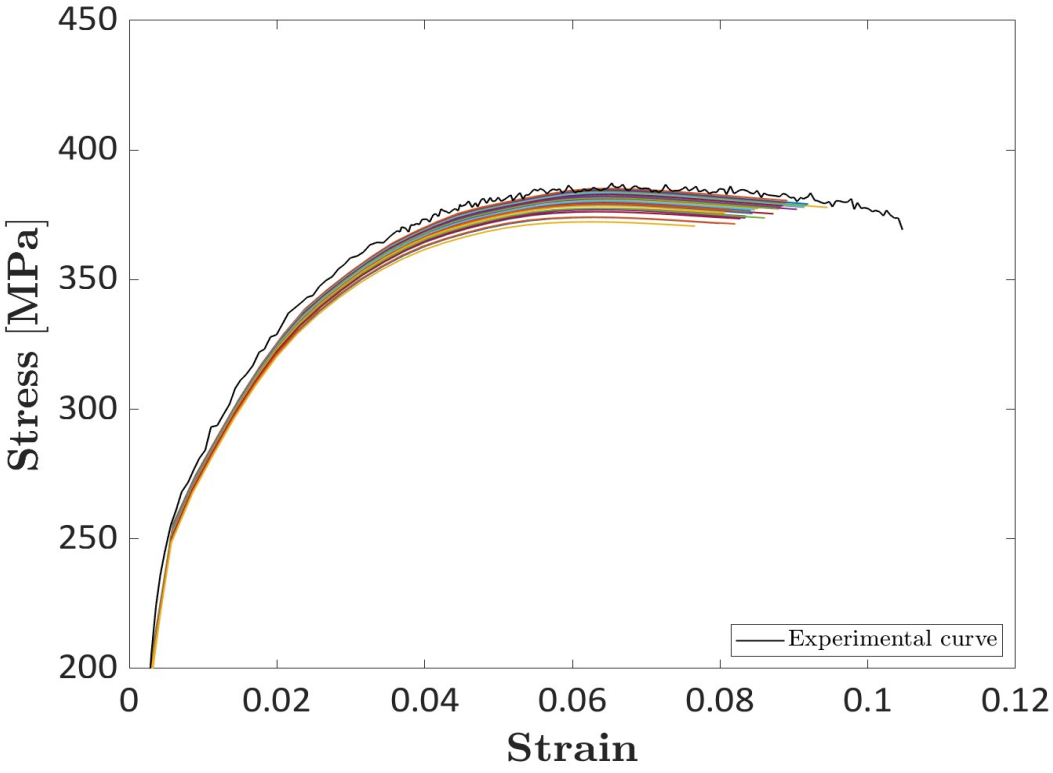

Figure 4.15. Stress-strain curve variabile RVE: new family of curves obtained with the updated class distribution

While an improvement has been achieved, the variability among the class curves is not so pronounced. Furthermore, having a cubic Representative Volume Element (RVE) of the same size as the structural beams can lead to an underestimation of the defect's influence, as there is more material than in the real case. As a result, the curves deviate less from the nominal value.

To address these issues, a cylindrical-shaped RVE representing a portion of the structural beam was concurrently analyzed.

4.2 Multiscale analysis with cylindrical RVE

As previously mentioned, the use of a cubic Representative Volume Element (RVE) at the micro-scale presents some challenges in this case. For the larger defect classes, the size of the RVE becomes comparable to that of the lattice structure's beams. Consequently, the assumptions of multi-scale analysis with periodic boundary conditions break down, and the square cross-section of the RVE is no longer comparable to the circular cross-section of the structural rods. Therefore, it is advisable to consider a second type of local-scale elements: 3D models of circular-section beams (cylindrical RVE).

4.2.1 Model geometry

The geometric model consists of a cylinder with a diameter of 1.31 mm (the actual diameter of the structural beam) and a height of 1 mm (corresponding to the mesh size at which the lattice structure of the sample will be discretized). Within this cylinder, spherical defects have been randomly placed, corresponding to the defect classes analyzed earlier (Figure 4.16).

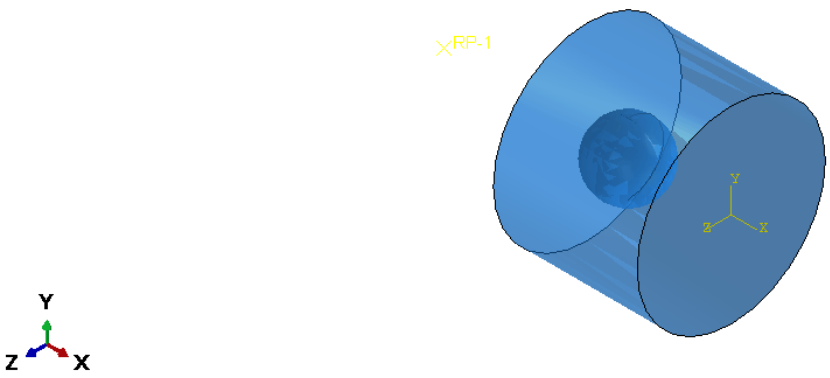

Figure 4.16 3D beam model with an internal spherical cavity created in Abaqus CAE

4.2.2 Boundary conditions

The loading and boundary conditions imposed on the element ensure compression of the model without restricting translations on the two faces, allowing them to expand freely during compression.

On one face of the cylinder, a symmetry constraint has been applied with respect to the axis of the cylinder. Unlike a fixed constraint, a symmetry constraint allows translation along the plane's axes while blocking rotations.

On the opposite face, a compressive displacement is applied. To achieve this, it was found that the best way to transmit the load to the face is by creating a rigid interaction between a master node, called the reference point, and all the nodes on the face. The reference point has been set to undergo a displacement of u1 = 0.1 mm in compression along the x-axis while all other translations and rotations are constrained (Figure 4.17).

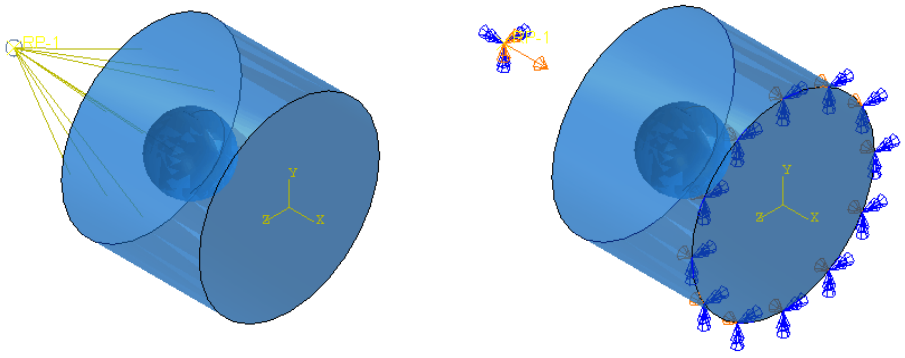

Figure 4.17 Creating rigid interaction with the face nodes and defining displacement boundary conditions

4.2.3 FE simulations

As in the previous case with the cubic RVE, finite element method (FEA) simulations were performed for each of the 38 defect classes discretized by the probability distribution of defects.

In Figure 4.18 and Figure 4.19, the contour plots on the cylindrical Representative Volume Element (RVE) are presented with results in terms of strain and stress, respectively.

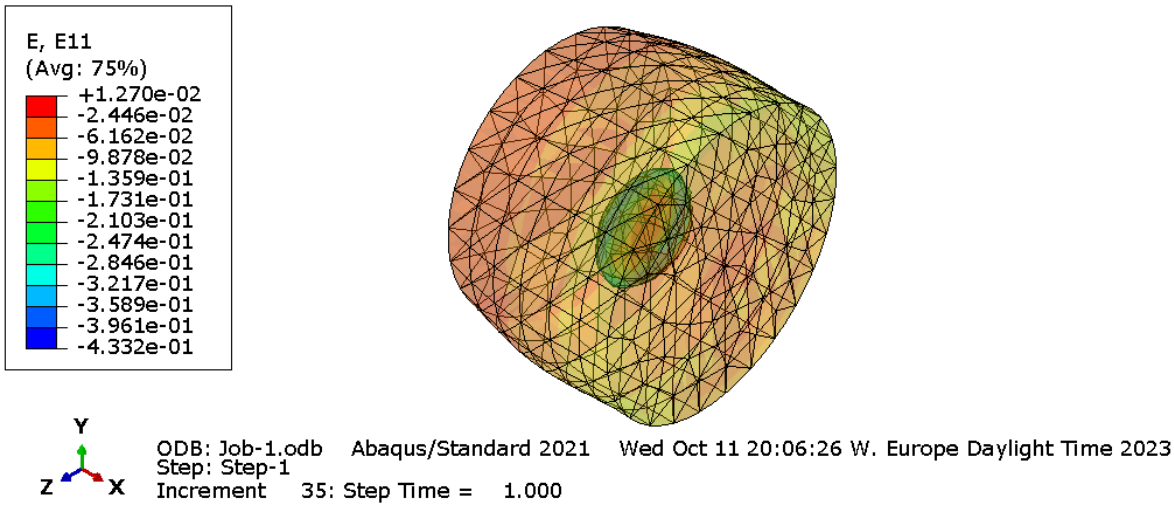

Figure 4.18 Deformed configuration of the beam with a contour plot of strain E11

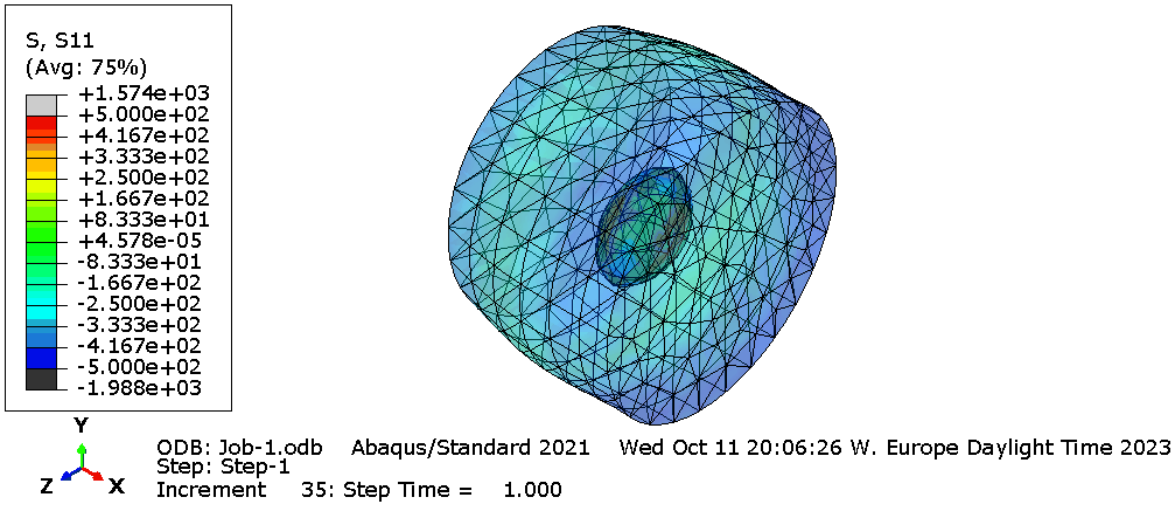

Figure 4.19 Deformed configuration of the beam with a contour plot of stress S11

Analyzing the deformation of the model, it is observed that the first elements to reach failure are those near the spherical void of the defect, as shown in Figure 4.20.

Also, it was determined that the shape of the beam is such that it does not produce distorted elements. Therefore, in this case, it was useful to analyze the threshold parameter for elements reaching failure relative to the total mesh elements. A sensitivity study was conducted, examining the variation of the maximum failure load as a function of the threshold value for elements reaching failure, while keeping the model of the beam with an internal defect fixed.

Keeping the diameter of the internal spherical cavity fixed (it was considered d = 0.312 mm, corresponding to the ID = 21 class), several FE simulations were repeated on the RVE, interrupting the writing of stress-strain values from the odb file for different fracture element threshold values.

As seen in Figure 4.21, there is a significant decrease in the maximum load as the threshold value increases.

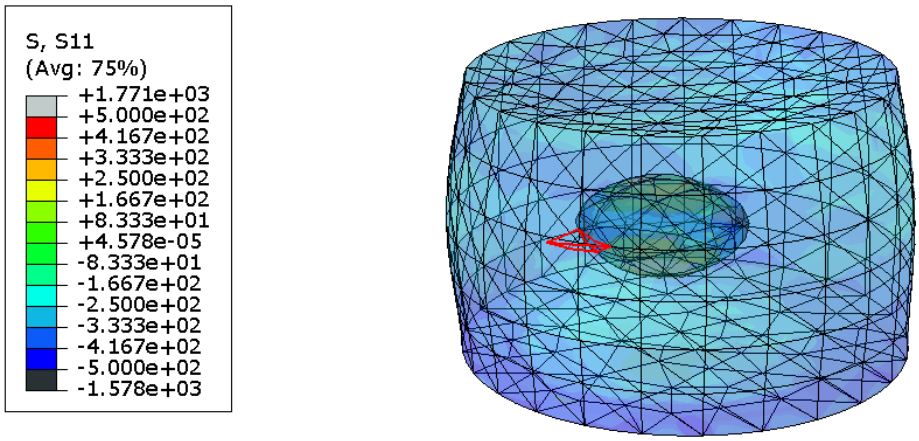

Figure 4.20 First element to fail within the beam near the spherical cavity

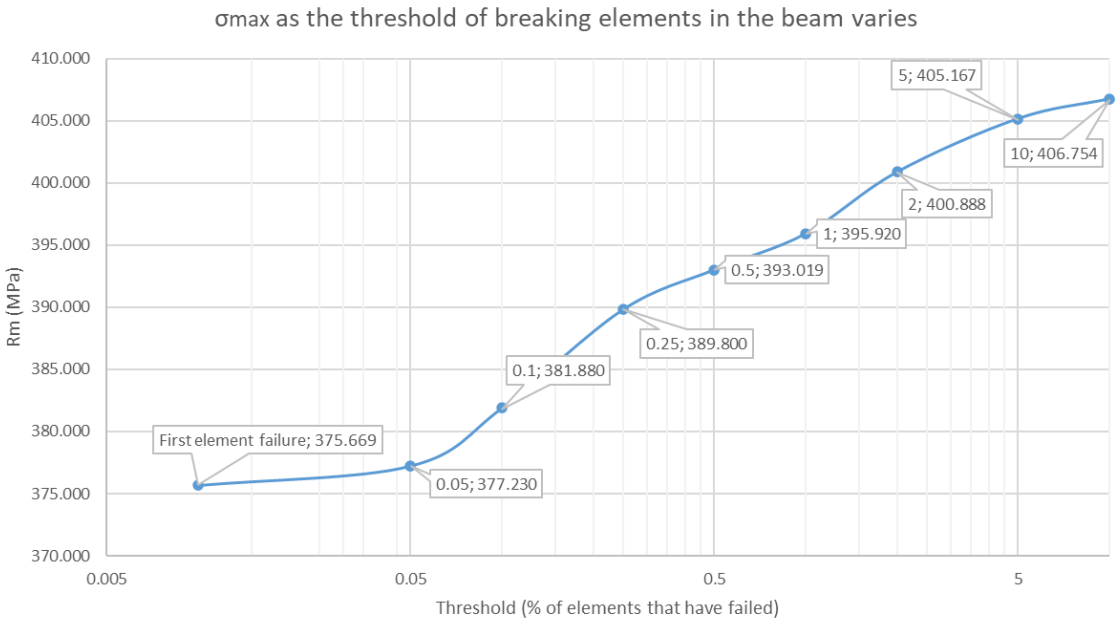

Figure 4.21 Variation of maximum stress with respect to the failure threshold of elements

As an example, the σ-ε curves for the defect classes, obtained by considering failure at the first mesh element of the model, are shown in Figure 4.22. It is noticeable that, at the same strain level, there is a decrease in the achieved stress and a greater variability between the curves compared to the case with the RVE.

Furthermore, there is an additional variability associated with the position of the spherical defect within the model: the positions of the sphere centers are randomly distributed within the material, but a defect closer to the edge results in the first mesh element failure occurring at lower stress and strain values compared to a scenario with a central defect.

These curves were subsequently used to define the material properties of each lattice structure element in the sample.

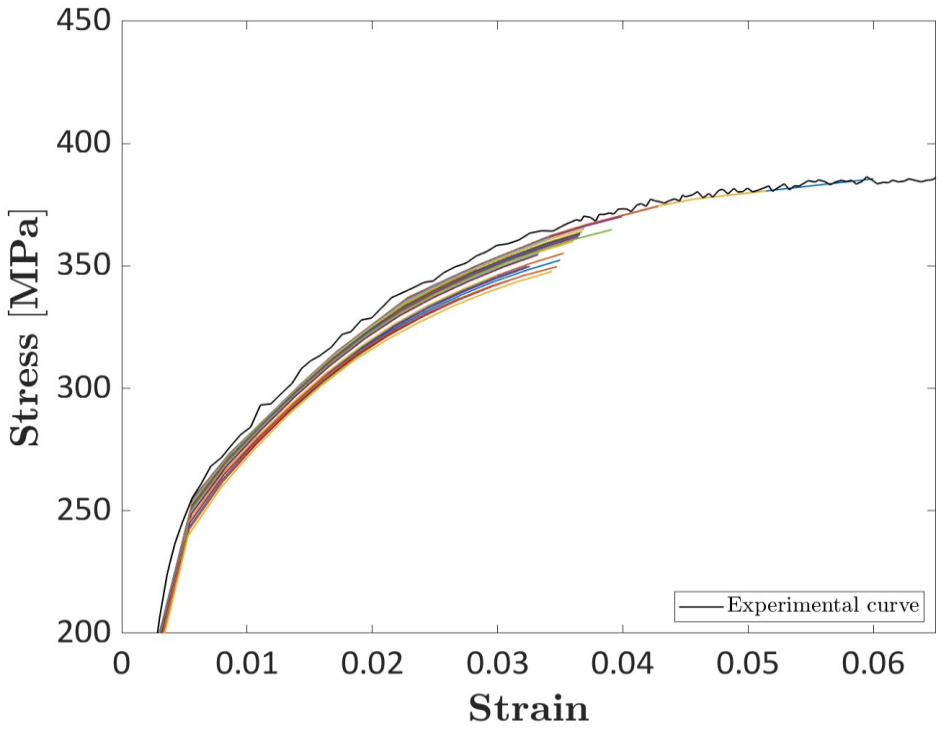

Figure 4.22 Distribution of σ-ε curves obtained using local-scale 3D cylindrical elements

Comparing the results obtained using cylindrical beam-type Representative Volume Elements (RVEs), it can be observed that the convergence of the fracture load as a function of the number of elements to failure leads to more accurate results compared to the case with cubic RVEs. In the case of cubic RVEs, the presence of distorted mesh elements could lead to inaccuracies in determining the maximum load. The most accurate condition is indeed achieved by interrupting the stress-strain curve when the first mesh element fails, and this can only be achieved using cylindrical RVEs.

Furthermore, cubic RVEs that reach a size equal to or greater than the beam diameter of the specimen do not provide a correct approximation of the problem at a local scale. Finally, when the strain is held constant, there is slightly more variability between the curves of different defect classes when using cylindrical RVEs.

For these reasons, curves obtained with cylindrical RVEs will be used to define the MATERIAL CARD in finite element simulations of the lattice structure model.

5 FEA Modeling of the influence of defects

The analyses carried out at the local scale on Representative Volume Elements (RVE) with defects allowed obtaining stress-strain curves dependent on each defect class of the distribution shown in Figure 3.13 and Figure 3.14.

The next step involves transitioning to the global scale to associate these properties with the lattice structure of the specimen.

The lattice structure consists of interconnected beams. These beams have a circular cross-section with a diameter of 1.31 mm.
The specimens analyzed have a cubic structure with dimensions of either 30 x 30 x 30 mm or 20 x 20 x 20 mm.

Using the FEA modeling software LS-Dyna, the lattice structure has been discretized with a 1D beam element mesh. Each element, which represents a section of the original beam, is defined in a CARD by various parameters, including section properties such as diameter, material properties, and node IDs connecting each element (Figure 5.1 and Figure 5.2).

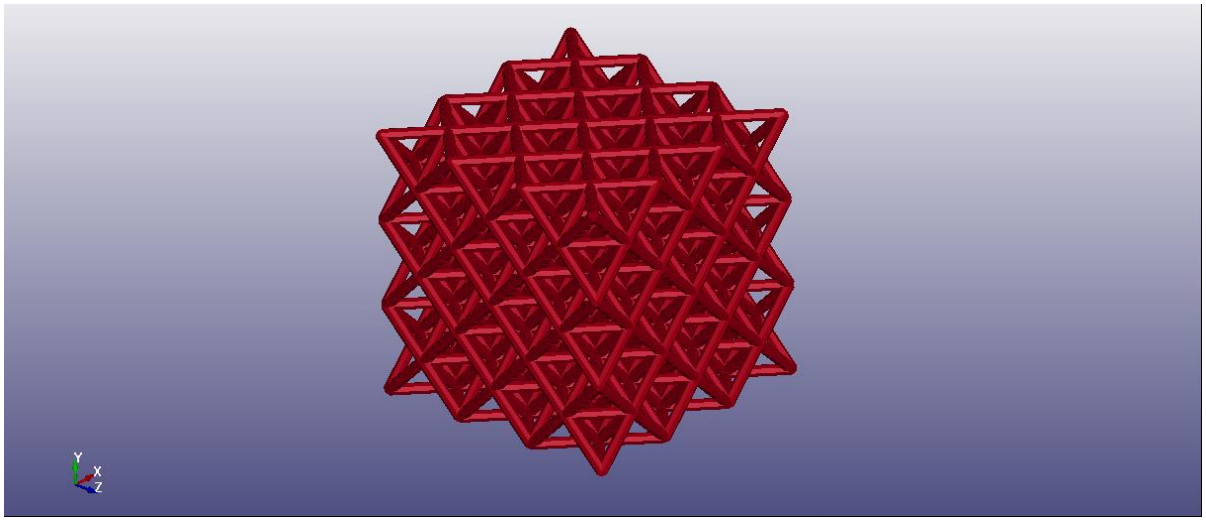

Figure 5.1. 3D model of the lattice specimen type 30 x 30 x 30 mm

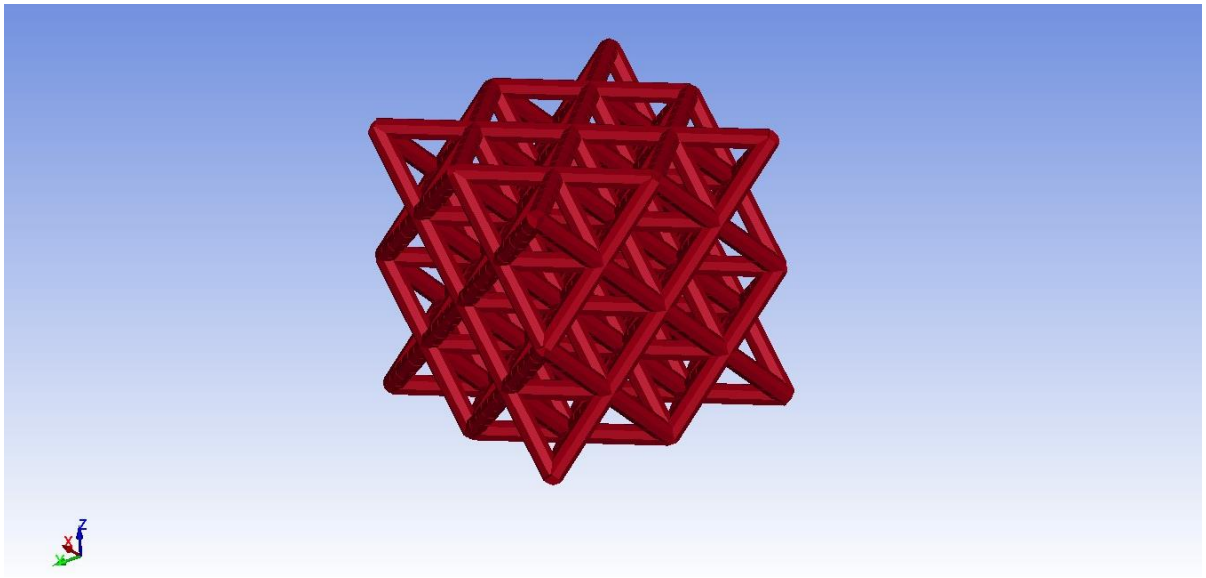

Figure 5.2 3D model of the lattice specimen type 20 x 20 x 20 mm

A fundamental aspect for the analysis is the method of dealing with internal defects within the structure's beams, as evidenced by Micro-CT scans performed on lattice specimens.

For this study, a multiscale approach was chosen to account for defects while remaining in a 3D element framework (RVE), and then extending the results to the global lattice structure. What was obtained from the simulations on the RVE are families of stress-strain curves that vary based on the defect class (spherical diameter) used in the FEA simulation. The defect classes, discretized according to the previously described experimental distribution, amount to 38 – one for each spherical defect diameter.

The goal is to associate a different material card with each element of the lattice structure, assigned randomly. The input consists of the point-based curve obtained from one of the RVE simulations with an internal defect of a specific class. There will be 38 material response curves to be randomly associated with each element through its respective material card. In this way, the presence of internal defects is assessed on a local scale using 3D elements, and the material response obtained is associated with the global lattice structure.

Pairs of stress-strain data obtained from Abaqus simulations for each defect class are collected in a supporting Excel file, which is then used as a basis for reading by a MATLAB function that generates Keyword files containing material, part, and element cards. The first one generated is the "material.k" file, containing diverse MATERIAL CARDs for each defect class.

In Figure 5.3, one of the 38 MATERIAL CARDs is shown, where the variables *mid* (material ID) and *lcss* vary incrementally, assuming the value of the defect class number. Another important parameter is *fail*, which is necessary for defining failure for each material card. It is analogous to the ultimate strain value for the curve. Therefore, for each card corresponding to a defect class, the corresponding ultimate strain value is inserted based on the material curve. This parameter can be adjusted later to achieve results that are closer to the experimental curve.

```
*KEYWORD
*MAT_PIECEWISE_LINEAR_PLASTICITY_TITLE
AlSi10Mg
$#     mid        ro         e        pr      sigy      etan      fail      tdel
         1  22.60000E-9   53000.0      0.33       0.0       0.0  0.119425       0.0
$#       c         p      lcss      lcsr        vp
       0.0       0.0         2         0       0.0
$$ HM Entries in Stress-Strain Curve =         8
$#    eps1      eps2      eps3      eps4      eps5      eps6      eps7      eps8
       0.0       0.0       0.0       0.0       0.0       0.0       0.0       0.0
$#    es1       es2       es3       es4       es5       es6       es7       es8
       0.0       0.0       0.0       0.0       0.0       0.0       0.0       0.0
```

Figure 5.3. Example of a card for a material class

The "material properties" card is linked to a stress-strain curve obtained from an RVE simulation. The MATLAB function reads the data points from the input Excel document containing the curves and writes the stress and strain values for the corresponding defect class into the "material.k" file, specifically in the DEFINE_CURVE section.

In the image below, the curve obtained for the first defect class is shown. The value of "lcid," to which "lcss" is linked, is indeed equal to 1.

However, the values inserted as points in the curves are not the same as those obtained from the RVE simulations. The former are engineering values, while in LS-Dyna, what is required are true stress and true strain values, related by the following equations:

$$\sigma_T = \sigma\,(1 + \varepsilon) \tag{5.1}$$

$$\varepsilon_T = \ln(1 + \varepsilon) \tag{5.2}$$

The stress-strain curves for all defect classes are then recalculated to assume true values.

In Figure 5.4, an excerpt from the Excel table is shown, containing all the True stress - True strain curves for data points in case of the first 5 defect classes analyzed using 3D beam elements.

Class 1		Class 2		Class 3		Class 4		Class 5	
Stress	Strain	Stress	Strain	Stress	Strain	Stress	Strain	Stress	Strain
151.4267	0.002857	151.421	0.002857	151.4114	0.002857	151.3842	0.002856	151.3559	0.002856
237.7552	0.005714	237.7504	0.005714	237.7425	0.005714	237.7044	0.005714	237.6365	0.005709
264.0294	0.008571	264.0264	0.008571	264.0239	0.008572	263.9916	0.008572	263.9185	0.008564
280.7144	0.011428	280.7118	0.011428	280.7111	0.011429	280.6783	0.011429	280.6049	0.011418
295.458	0.014285	295.4547	0.014285	295.4537	0.014286	295.4171	0.014286	295.3461	0.014273
310.108	0.017142	310.1041	0.017142	310.1021	0.017144	310.0604	0.017143	309.9874	0.017128
323.3641	0.019999	323.3604	0.019999	323.3592	0.020001	323.3165	0.020000	323.2383	0.019983
335.3179	0.022857	335.3134	0.022856	335.3106	0.022858	335.2617	0.022857	335.1835	0.022838
346.2483	0.025714	346.2449	0.025713	346.2452	0.025716	346.1984	0.025716	346.1064	0.025693
354.0518	0.028571	354.0488	0.02857	354.0493	0.028573	354.0017	0.028573	353.9129	0.028547
361.5366	0.031428	361.5337	0.031427	361.5353	0.031431	361.487	0.031431	361.3969	0.031402
368.4914	0.034285	368.4881	0.034284	368.4886	0.034288	368.4362	0.034288	368.3457	0.034257
375.4451	0.037142	375.44	0.037142	375.4358	0.037146	375.3666	0.037145	375.2614	0.037111
380.6888	0.039999	380.6865	0.039999	380.6902	0.040004	380.6387	0.040004	380.5408	0.039966
385.5959	0.042856	385.5933	0.042856	385.5957	0.042861	385.54	0.042861	385.441	0.042821
390.5022	0.045713	390.4983	0.045713	390.4972	0.045719	390.4296	0.045719	390.3166	0.045675
394.1994	0.04857	394.1985	0.04857					394.0587	0.048533
396.9796	0.051427	396.9791	0.051427						
399.7595	0.054284								
402.5392	0.057141								

Figure 5.4. Pairs of points of true stress - true strain for the first 5 defect classes (failure at the first element)

Another parameter that has been appropriately adjusted is the *offa* parameter, which represents the elastic strain at yield expressed with a negative sign. Like the *fail* parameter, this value is not consistent across all classes but undergoes some variations for each curve.

Finally, the deformation values used by the solver are exclusively the components of plastic deformation (plastic strain) of the material. Therefore, it was necessary to subtract the value of *offa* from the total deformation data.

For each of the DEFINE CURVE associated with one of the MATERIAL CARD with the parameter *lcss*, it can be obtained a card as shown in Figure 5.5. The x-axis column (*a1*) corresponds to the true strain values, while the y-axis (*o1*) represents the respective true stress values for the RVE class.

```
*DEFINE_CURVE_TITLE
Plastic_Sig-Eps_Aluminum_3D
$#     lcid      sidr       sfa       sfo      offa      offo    dattyp     lcint
         2         0       1.0       1.0 -0.002857       0.0         0         0
$#               a1                  o1
          0.002857          151.426677
          0.005714          237.755188
          0.008571          264.029358
          0.011428          280.714385
          0.014285          295.457958
          0.017142          310.107952
          0.019999          323.364123
          0.022857          335.317856
          0.025714          346.248301
          0.028571          354.051850
          0.031428          361.536568
          0.034285          368.491393
          0.037142          375.445077
          0.039999          380.688814
          0.042856          385.595920
          0.045713          390.502206
          0.048570          394.199420
          0.051427          396.979640
          0.054284          399.759530
          0.057141          402.539250
```

Figure 5.5. Example card with curve parameters for a material class

Subsequently, the MATLAB function generates a "part.k" file where the created material cards are uniquely associated with each part.

In Figure 5.6, the card for the first part is depicted with a *pid* (part ID) of 1, corresponding to the first defect class. A unique "mid" (material ID) of 1 is associated with *pid* = 1. The subsequent cards increment both *pid* and *mid* in the same manner until reaching the last defect class.

What remains constant in this case is the "section ID" (*secid*): there is only one for all parts (and all elements) as the diameter of the beam remains constant at 1.31 mm.

```
*KEYWORD
*PART
$HWCOLOR COMPS       1       3
$#                                                                  title
MESH_Unit_Cell_04_3x3
$#     pid     secid       mid     eosid      hgid      grav    adpopt      tmid
         1         1         1         0         0         0         0         0
```

Figure 5.6. Example of linking a material card to a part card for a class

In the "part.k" file, a card related to the Set Part is also automatically included through the script. This card contains the identifiers of all parts (all 38 part IDs) and ensures the contact between all the beams during the analysis, as they are interconnected with each other (Figure 5.7).

```
*SET_PART_LIST_TITLE
Effective_beams
$#     sid       da1       da2       da3       da4    solver
         1       0.0       0.0       0.0       0.0MECH
$#    pid1      pid2      pid3      pid4      pid5      pid6      pid7      pid8
         1         2         3         4         5         6         7         8
         9        10        11        12        13        14        15        16
        17        18        19        20        21        22        23        24
        25        26        27        28        29        30        31        32
        33        34        35        36        37        38         0         0
*END
```

Figure 5.7. Creation of the part set containing all part cards

Finally, a "element_beam.k" file is created where, with each generation, the value of the "pid" (part id) is modified for each "elid" (element id). The "pid" value is assigned a value between 1 and 38, corresponding to a material card of

a defect class, and the assignment is proportional to each class's probability level. This is accomplished through a script using MATLAB's "randsample" function:

```
% Definition of probabilities for each value of PID
probability = [0.0137, 0.0142, 0.0453, 0.0477, 0.069, 0.056, 0.065, 0.067,
0.056,0.093,0.084, 0.072,0.069,0.037,0.039,0.026,0.018,0.018,0.012, 0.01,
0.009,
 0.006, 0.007, 0.005, 0.0045, 0.004, 0.003, 0.0024, 0.00277, 0.00191,
0.00204, 0.00139, 0.00123, 0.00118,0.00092, 0.00102, 0.00073, 0.00071];

% Generation of the PID(k) values based on the probabilities
pid = randsample(2:(n_classi+1), total_elements, true, probability);
```

Pid array, which has a length equal to the number of elements, assigns to each value a random but weighted class of defect number based on its probability of occurrence. The focus is shown in Figure 5.8 on some model elements, where the association of each element with a "pid" value ranging from 1 to 38 can be observed, following the probability of each class.

```
*KEYWORD
*ELEMENT_BEAM
$#    eid     pid      n1      n2      n3     rt1     rr1     rt2     rr2   local
     163      12     352     353       0       0       0       0       0       2
     164      11     353     355       0       0       0       0       0       2
     165       1     355     357       0       0       0       0       0       2
     166       7     357     359       0       0       0       0       0       2
     167       8     359     361       0       0       0       0       0       2
     168       5     361     194       0       0       0       0       0       2
     223       3     482     483       0       0       0       0       0       2
     224      10     483     485       0       0       0       0       0       2
     225       8     485     487       0       0       0       0       0       2
     226      15     487     489       0       0       0       0       0       2
     227      10     489     491       0       0       0       0       0       2
     228      15     491     194       0       0       0       0       0       2
     325      10     703     704       0       0       0       0       0       2
     326       1     704     706       0       0       0       0       0       2
     327       1     706     708       0       0       0       0       0       2
     328       5     708     710       0       0       0       0       0       2
     329       8     710     712       0       0       0       0       0       2
     330      13     712     714       0       0       0       0       0       2
     373       5     482     808       0       0       0       0       0       2
     374       7     808     810       0       0       0       0       0       2
```

Figure 5.8. Extract of the 'element_beam.k' file with random association of a PID to each element

The tests performed on the specimen in Ls-Dyna involve a quasi-static compression tests. These tests are conducted by applying a displacements to a rigid wall in contact with the specimen. The output evaluated from these tests consists of Force-Displacement curves.

By conducting a series of tests by considering random material cards within the model, indirectly accounting for the presence and positions of defects in the specimen, a family of Force-Displacement curves is generated.

The positions of the defects can significantly influence the material's response. For instance, the presence of a larger internal porosity might have a greater impact if it is situated at the edges or at the junctions between two beams, where stress concentrations are higher.

Through the use of an INCLUDE statement, these new files are referenced in the main keyword file. By importing this file into Ls-Dyna, the structure of the

specimen with material cards connected to each element is obtained. In Figure 5.9 and Figure 5.10, each element resulting from the discretization of the specimen's beams is color-coded to represent one of the 38 associated material cards.

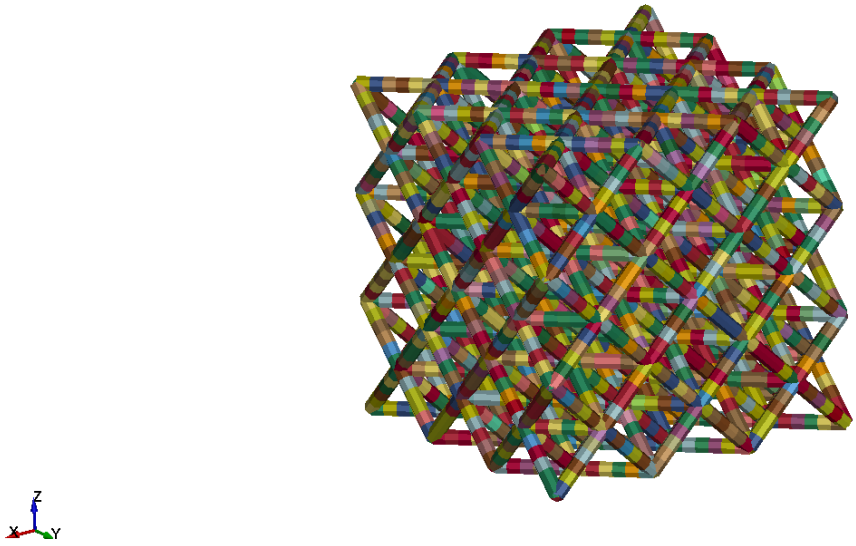

Figure 5.9. Association of a different material card to each beam segment: different colors correspond to different MID (30 x 30 mm cell)

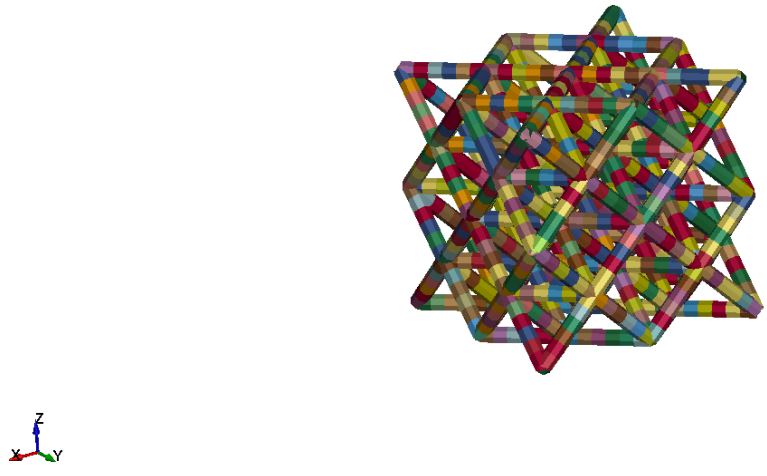

Figure 5.10. Association of a different material card to each beam segment: different colors correspond to different MID (20 x 20 mm cell)

As observed, all 38 material cards associated with each element have been successfully imported (Figure 5.11).

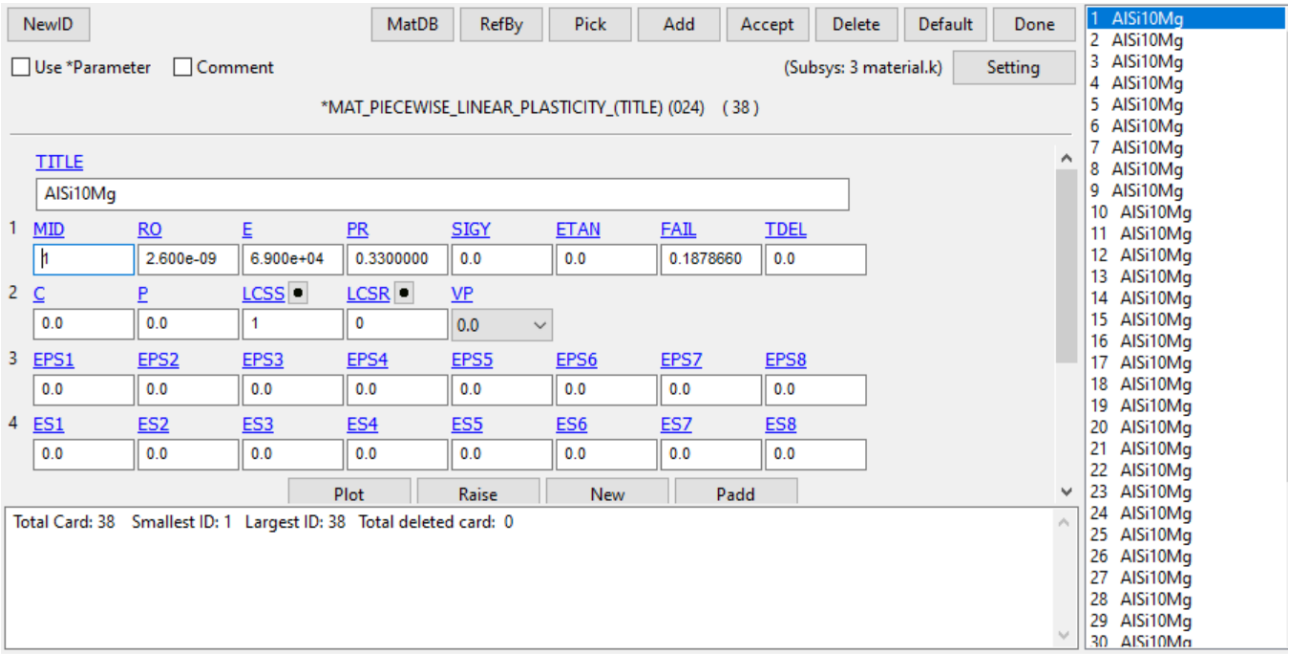

Figure 5.11. Visualization of properties for a material card in LS-DYNA

The specimen created in LS-Dyna must numerically simulate the quasi-static compression mechanical behavior experienced by the real specimen.

To simulate the compression tests on the specimen, two parallel rigid walls were created in contact with the specimen. The lower wall, which remains fixed, is common to both types of tests and was used to replicate the support plane. This lower wall was defined using the card "RIGIDWALL_GEOMETRIC_FLAT_DISPLAY." (Figure 5.12).

```
*RIGIDWALL_GEOMETRIC_FLAT_DISPLAY_ID
$HWCOLOR RIGIDWALLS       2       4
$#      id                                                                title
         2Rwall_Lower
$#    nsid    nsidex     boxid     birth     death
         0         0         0       0.01.00000E20
$#      xt        yt        zt        xh        yh        zh      fric
     -15.0     -15.0      -0.7     -15.0     -15.0       0.0       0.3
$#    xhev      yhev      zhev      lenl      lenm
     -14.0     -15.0      -0.7      30.0      30.0
$#     pid        ro         e        pr
         01.00000E-91.00000E-4       0.3
```

Figure 5.12. Quasi-static case: card for the fixed upper Rigid wall

For the quasi-static test, the upper rigid wall was defined using the "RIGIDWALL_GEOMETRIC_FLAT_MOTION_DISPLAY" card. A linear displacement law was imposed on this upper wall (Figure 5.13).

```
*RIGIDWALL_GEOMETRIC_FLAT_MOTION_DISPLAY_ID
$HWCOLOR RIGIDWALLS       1       3
$#      id                                                                title
         1Rigid_Wall
$#    nsid    nsidex     boxid     birth     death
         0         0         0       0.01.00000E20
$#      xt        yt        zt        xh        yh        zh      fric
     -15.0     -15.0     26.25     -15.0     -15.0      26.0       0.1
$#    xhev      yhev      zhev      lenl      lenm
     -15.0     -14.0     26.25      30.0      30.0
$#    lcid       opt        vx        vy        vz
         1         1       0.0       0.0      -1.0
$#     pid        ro         e        pr
         01.00000E-91.00000E-4       0.3
```

Figure 5.13. Quasi-static case: card for the lower rigid wall with linear displacement

This law was included in a separate DEFINE_CURVE compared to the ones used for the material cards of the elements, and it was assigned an LCID value of 1 (Figure 5.14). Therefore, it was decided to vary the IDs of the material cards for the classes from the value 2 up to 39.

```
*DEFINE_CURVE_TITLE
Linear_Displacement
$#     lcid      sidr       sfa       sfo      offa      offo    dattyp     lcint
         1         0    0.0275      27.5       0.0       0.0         0         0
$#                 a1                  o1
                  0.0                 0.0
                  1.0                 1.0
```

Figure 5.14. Definition of linear displacement for the lower rigid wall: Assigning an LCSS value of 1

A series of tests is performed, and for each test, the element_beam.k file is progressively generated to carry out a new association between element id and part id. This approach allows us to determine a family of curves, one for each test conducted, that defines a range of variability for the material's response.

In Figure 5.15 the specimen is shown undergoing the described quasi-static compression test.

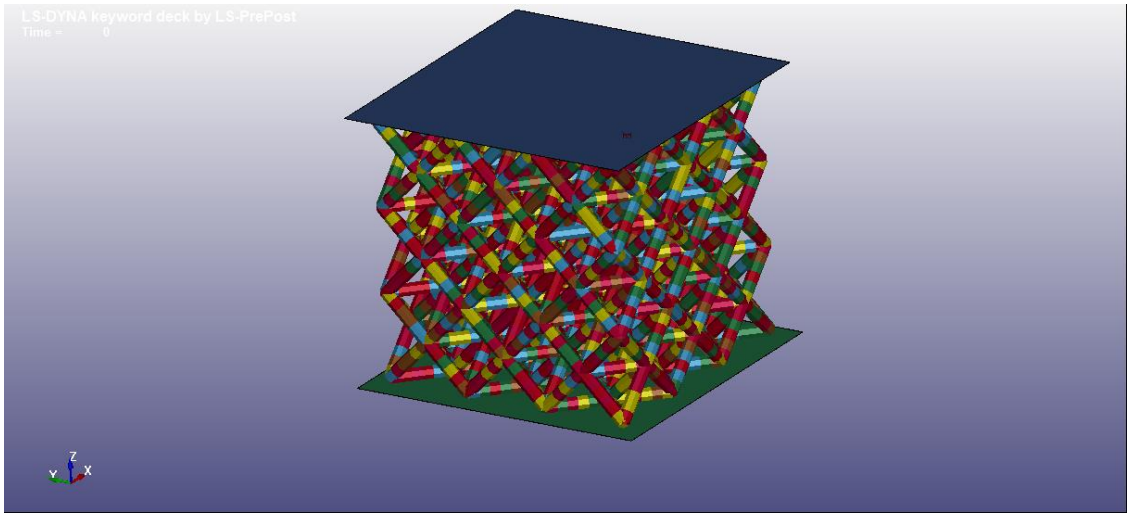

Figure 5.15. 3D model of the test specimen for the quasi-static compression case with the presence of the two RIGID WALLS, fixed and movable (30 x 30 mm cell)

6 Finite Element Analysis on the specimen

The final stage of the process involves performing Finite Element Analysis (FEA) on lattice specimen models in LS-Dyna, followed by comparing the numerical force-displacement response with the experimental material response. Figure 6.1 shows the flow chart summarizing the steps taken in the design of the model with a multiscale approach.

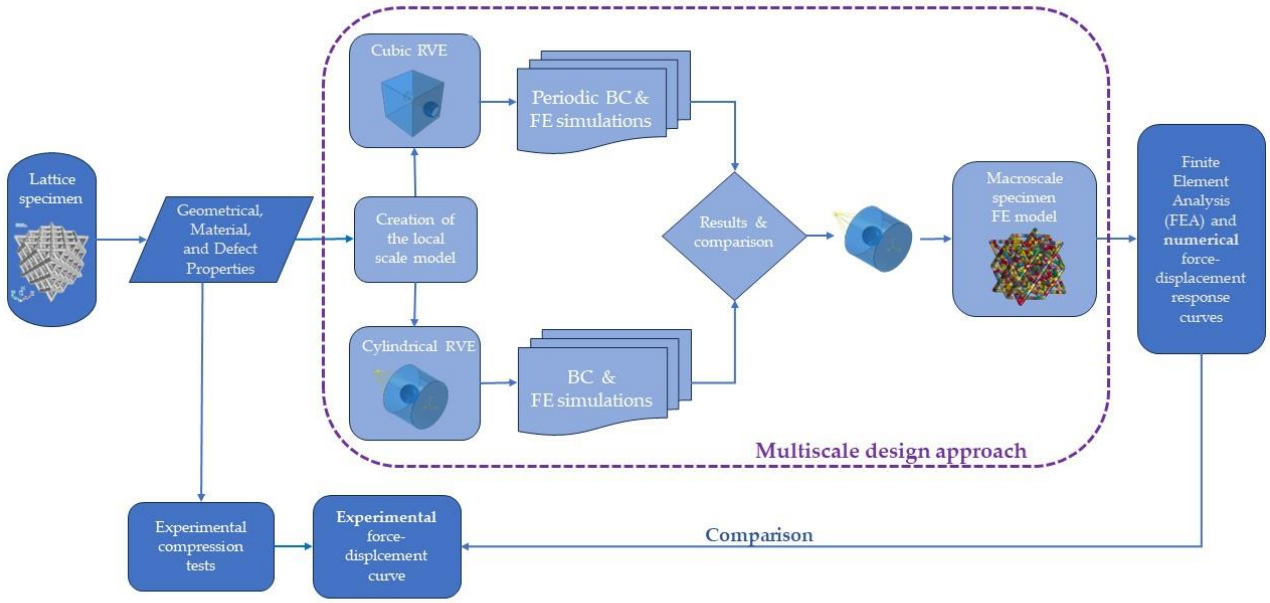

Figure 6.1. Representative flow chart of the steps performed for the creation of the finite element model with a multiscale approach

The Force-Displacement curves for the 30 x 30 x 30 mm and 20 x 20 x 20 mm cubic cells, as shown in Figure 6.2, have been obtained experimentally.

While the curve related to the test on the 20 x 20 mm cell was interrupted beyond the first force peak, the one for the 30 x 30 mm cell was allowed to

continue even for larger displacements. However, this portion of the curve is not necessary for the analysis since it depends solely on the densification stage occurring during compression.

Even after reaching structural failure, the structure continues to densify in the remaining space, resulting in an increase of the force in the terminal area of the curve. At the peak force, the fracture of a primary structural beam occurs, followed by numerous small fractures of other beams, producing a segmented pattern in the curve.

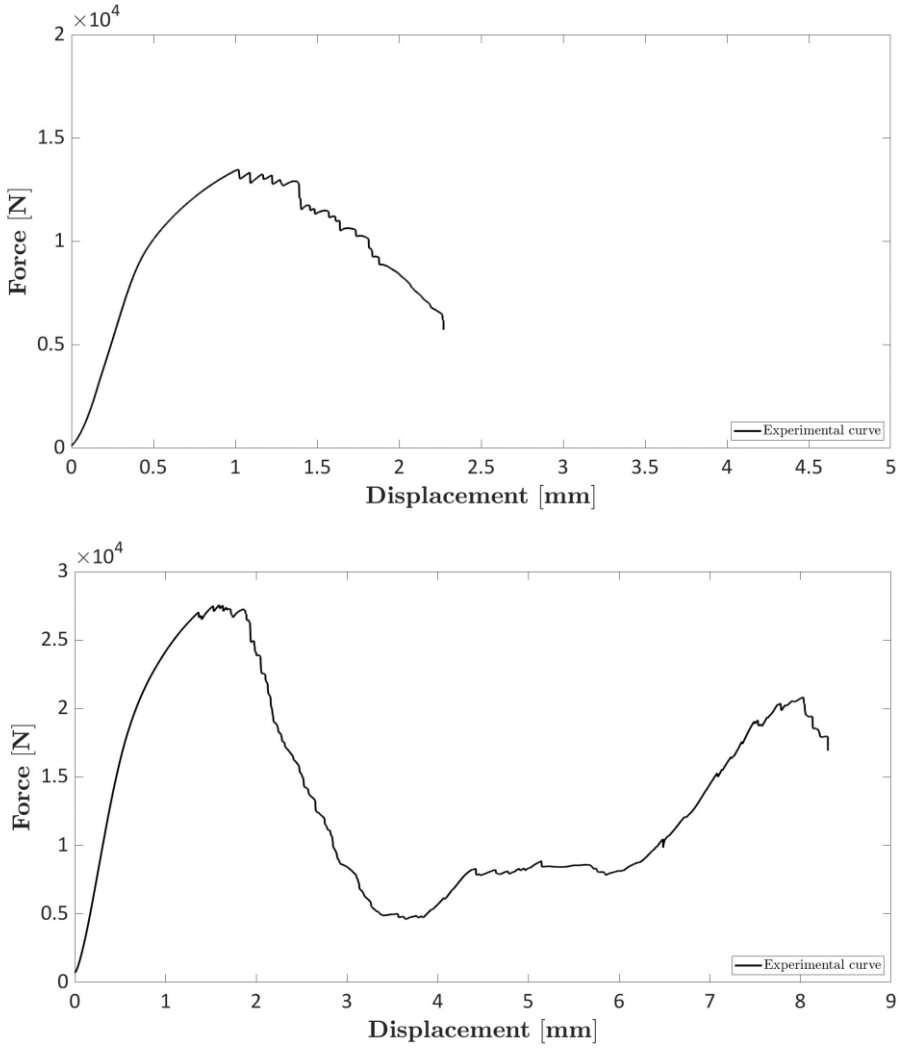

Figure 6.2 Experimental curves obtained from quasi-static compression tests on specimens with respectively 20x20 mm and 30x30 mm cells

Subsequently, numerical FE simulations were conducted, randomizing the material.k, element_beam.k, and part.k files each time, as explained in Chapter 5. Running the FE simulations in Ls-Dyna generates d3plot files containing the results of the analyses.

In Figure 6.3, for three frames of the FE simulation are reported, together with the contour plot depicting the axial beam stress distribution on the specimen with a cubic lattice structure of 30 x 30 x 30 mm. It can be observed that the specimen is in an overall compressive state, causing some beams to experience tension while others undergo compression. This ultimately leads to failure after a small phase of plastic deformation.

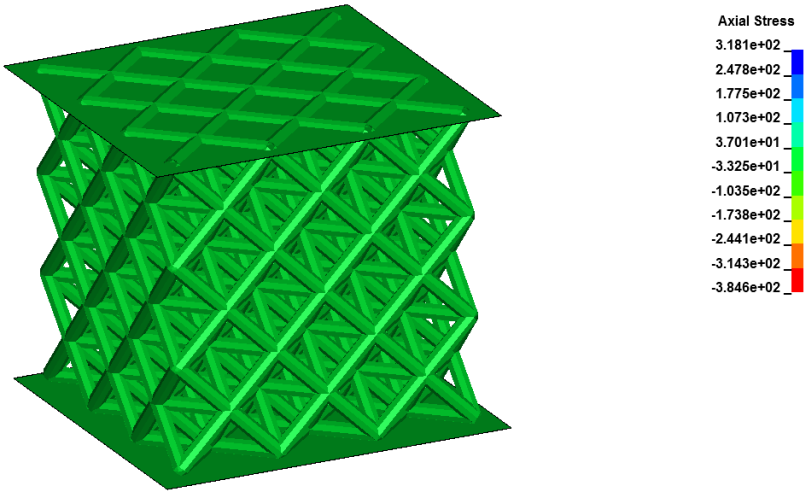

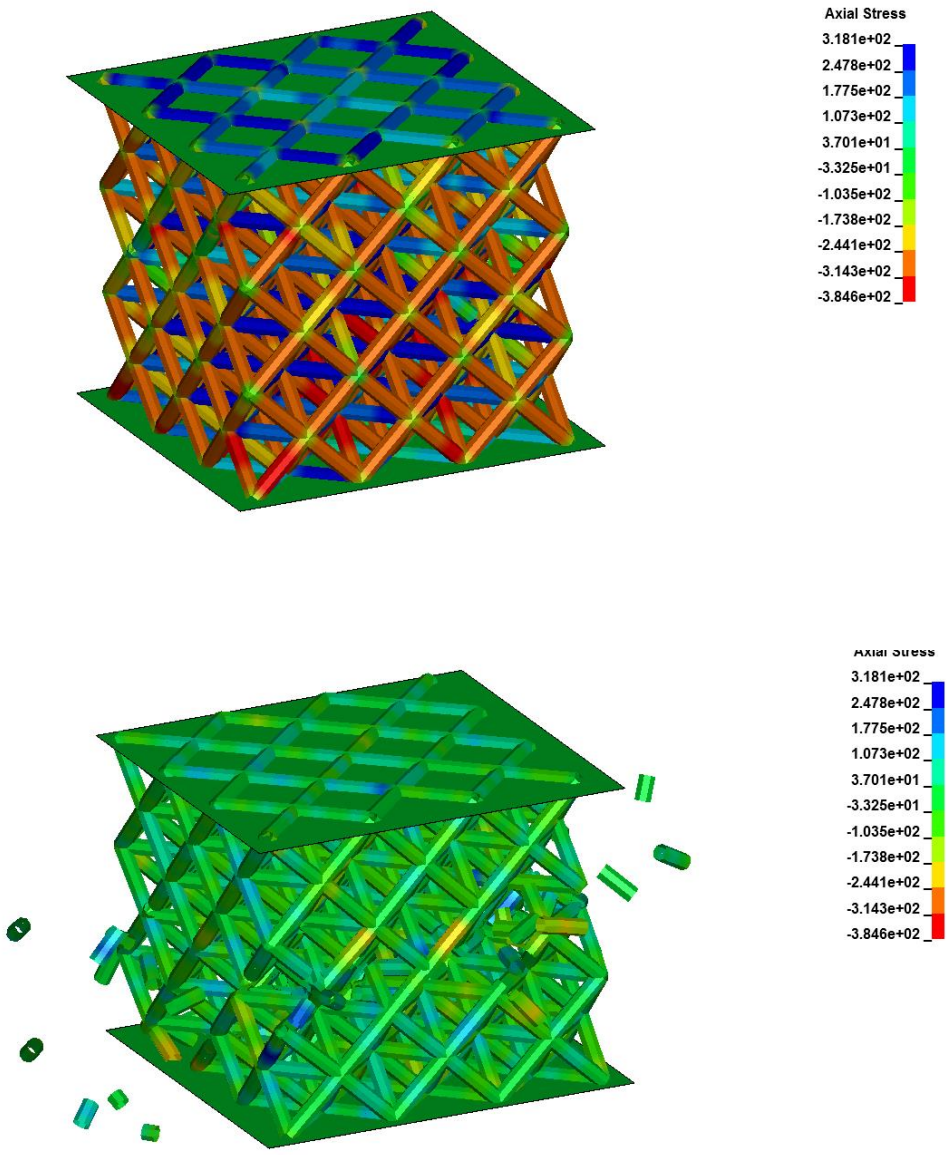

Figure 6.3.Compression of the test specimen in 3 successive simulation frames with reference to axial beam stress

The maximum force value attained is depicted in the frame of the d3plot, as shown in the middle frame of Figure 6.2, where the maximum deformation of the beams is observed before reaching failure. It is possible to generate the force vs. time curve by loading the binout file using the DATABASE_RWFORCE card. This card allows the extraction and analysis of force development on the

mobile rigid wall as a function of time: a $dt = 10^{-5}\, s$ was set to obtain a smoother curve without significantly impacting the computation.

In Ls-Dyna, by combining the force and displacement plots of the rigid wall (exhibiting a linear trend) as a function of time, it was possible to obtain the numerical force-displacement curve represented in Figure 6.4. The trend is associated with a lattice model of size 20 x 20 mm.

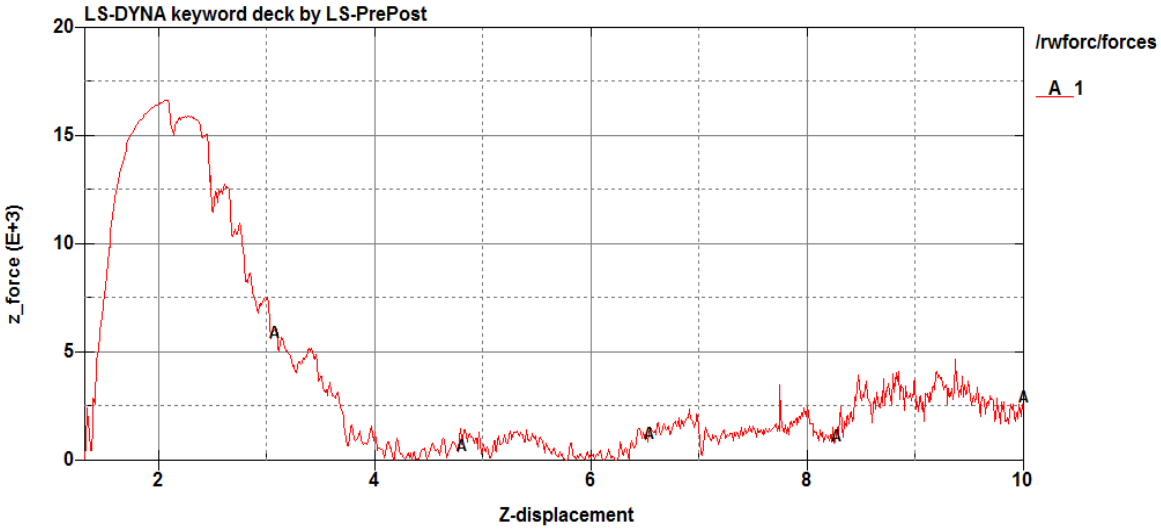

Figure 6.4 Force-displacement curve for a defect-free case on a 20x20 mm cell, unfiltered

As it can be observed, there is still a lot of noise resulting in an oscillatory pattern. A cosine filter with a frequency of 108 Hz was applied to reduce these disturbances, resulting in the curve shown in Figure 6.5.

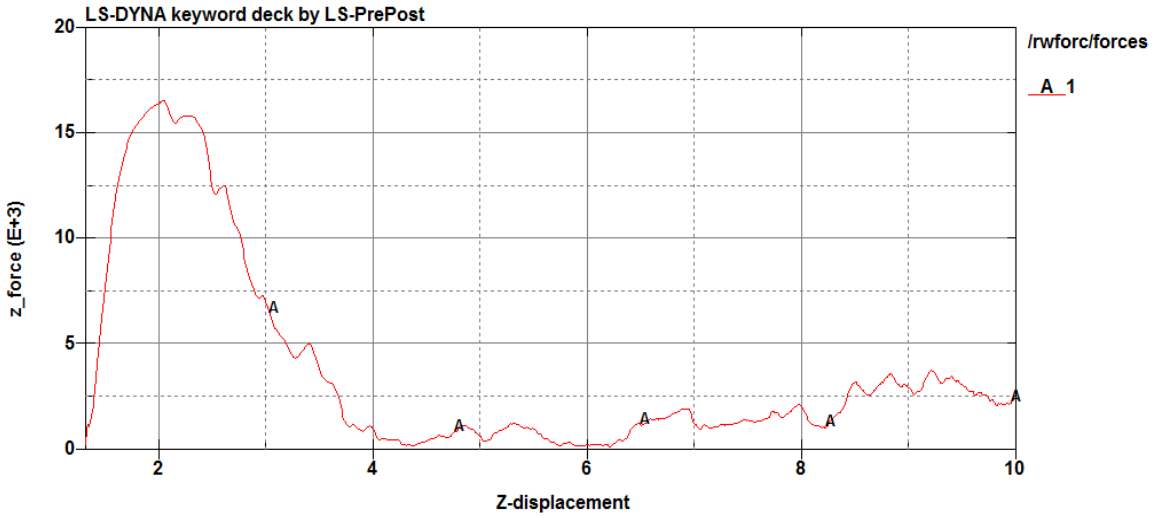

Figure 6.5 Force-displacement curve for case without defects (20x20 mm cell), with a cosine filter at 108 Hz

By creating new associations between material cards and beam elements, a series of simulations on the test specimen have been carried out to obtain a set of force-displacement curves. Subsequently, a comparison has been made between these numerical curves obtained from FEA analysis and the curve obtained experimentally with a quasi-static compression test conducted in laboratory.

In Figure 6.6, an initial comparison in terms of Force-Displacement curves between numerical simulation and experimental test (black curve) is shown. In order to assess the model's behavior, the presence of defects was not considered in the initial analysis. In fact, a single material card corresponding to the defect-free reference curve was assigned to all elements. The curves were truncated at a displacement of 4 mm, as the subsequent portion of the curve is not pertinent to the study.

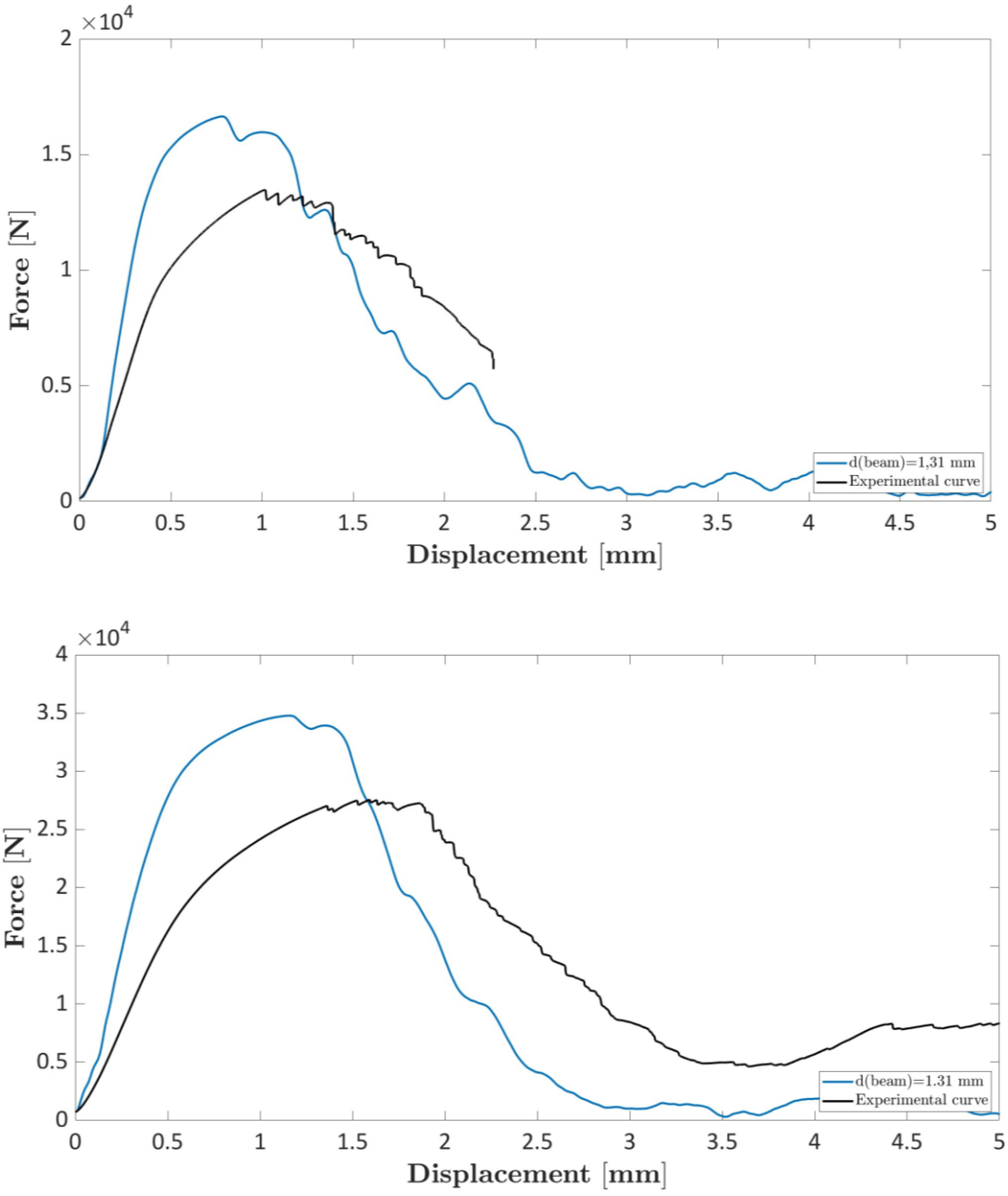

Figure 6.6 Comparison between the experimental curve and the numerical curve for a nominal beam diameter of d=1.31 mm. Above: on a 20 x 20 mm cell. Below: on a 30 x 30 mm cell

Firstly, it is immediately evident that the model's force behavior reaches higher peak values compared to the experimental specimen in both cases. Consequently, a more detailed analysis of the problem was deemed necessary.

As already indicated in Figure 3.10, the diameters of the beams in the specimen exhibit some variability, as measured under an electron microscope. Additionally, the presence of internal defects within the lattice structure is known to contribute to the reduction of the specimen's mass.

In the study *Mechanical equivalent diameter of single struts for the stiffness prediction of lattice structures produced by Electron Beam Melting* [8], the variability of the experimental beam diameter in generating the Finite Element Analysis (FEA) model of lattice structure was analyzed. Beams produced through Additive Manufacturing processes exhibit low dimensional accuracy. Therefore, in accordance with the study, an analysis was conducted to determine a representative beam diameter (d_beam) for the FE model, taking into account the dimensional variations introduced by the production process and internal defects.

In the first step, the two specimens with cell dimensions of 20 x 20 mm and 30 x 30 mm were weighed, yielding the following masses: $m_{3x3} = 14{,}58\ g$ e $m_{2x2} = 4{,}87\ g$.

An analysis was conducted to determine the effective beam diameter to be considered for the model. With a nominal diameter of 1.31 mm, the mass of the model can be overestimated due to the presence of mass portions that do not actively contribute to the load.

As a result, a minimum limit diameter for the lattice specimen model in Ls-Dyna was established to ensure an equivalent mass to that of the actual specimen. This convergence study led to the following beam diameters: $d_{3x3} = 1{,}0485\ mm$ e $d_{2x2} = 1{,}017\ mm$.

The force-displacement curves obtained by simulating the 20 x 20 mm and 30 x 30 mm cells are illustrated in Figure 6.7.

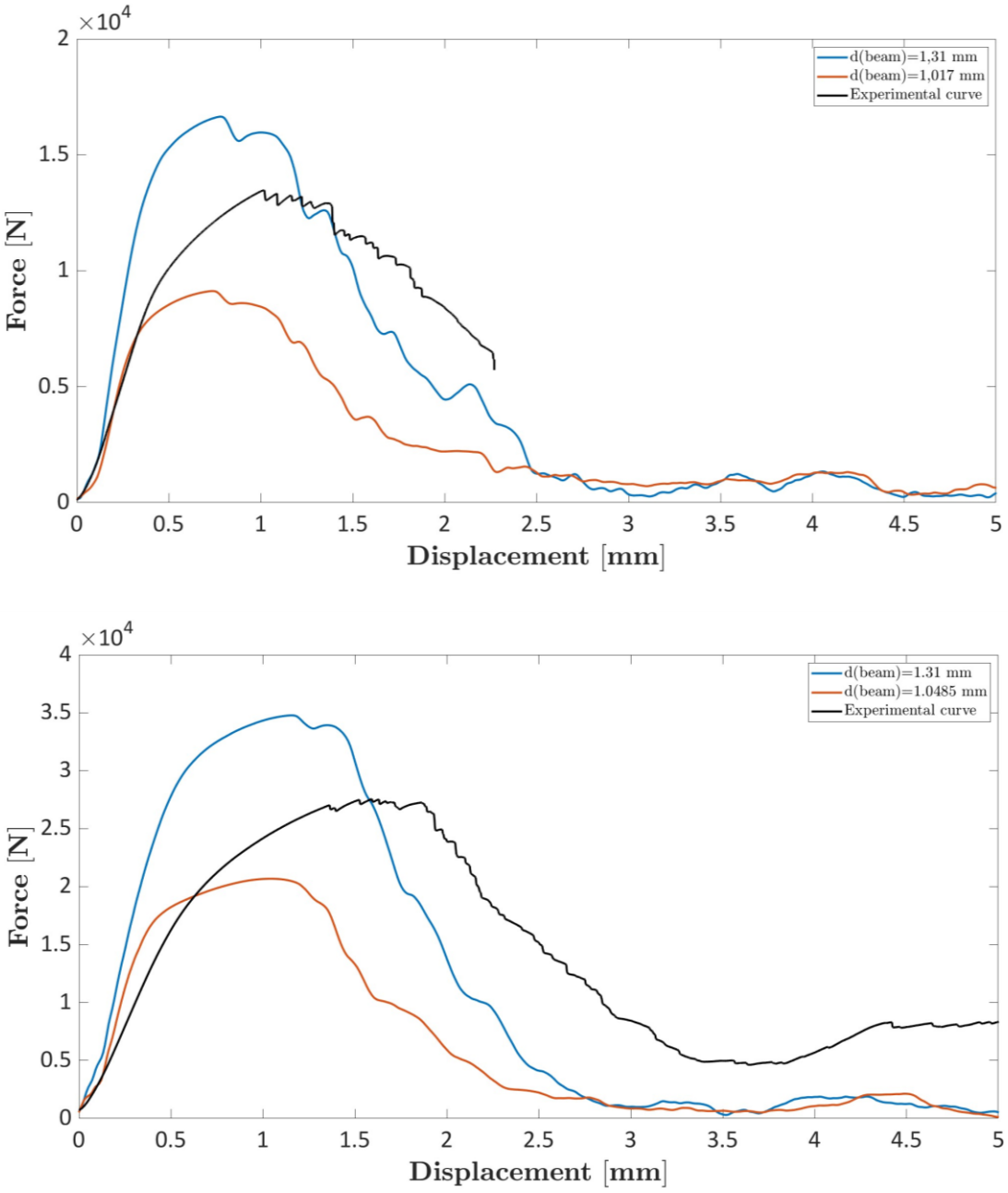

Figure 6.7 Numerical force-displacement comparison curves between the diameter d=1.31 mm and the minimum diameter achieving the same mass as the real specimen. The upper graph corresponds to the 20 x 20 mm cell, while the lower graph corresponds to the 30 x 30 mm cell

However, it is observed that, although the stiffness approximates well in the elastic region, the peak force reached is significantly lower than the

experimental one. Additionally, the diameter of the beams must be the same for both specimens. Therefore, a convergence study on the beam diameter was conducted to achieve a value that matched the experimental peak force while maintaining an acceptable stiffness.

The analyses were initially performed on the cubic cell model of 20 x 20 x 20 mm, given its lower computational cost for FE simulations. The analyses led to an effective beam diameter for the model equal to $d_{beam} = 1{,}2\ mm$. Once this diameter was calibrated for the 20 x 20 mm cell, the model for the 30 x 30 mm cell with the same beam diameter was validated.

The force-displacement response obtained from the FE simulations is shown in Figure 6.8.

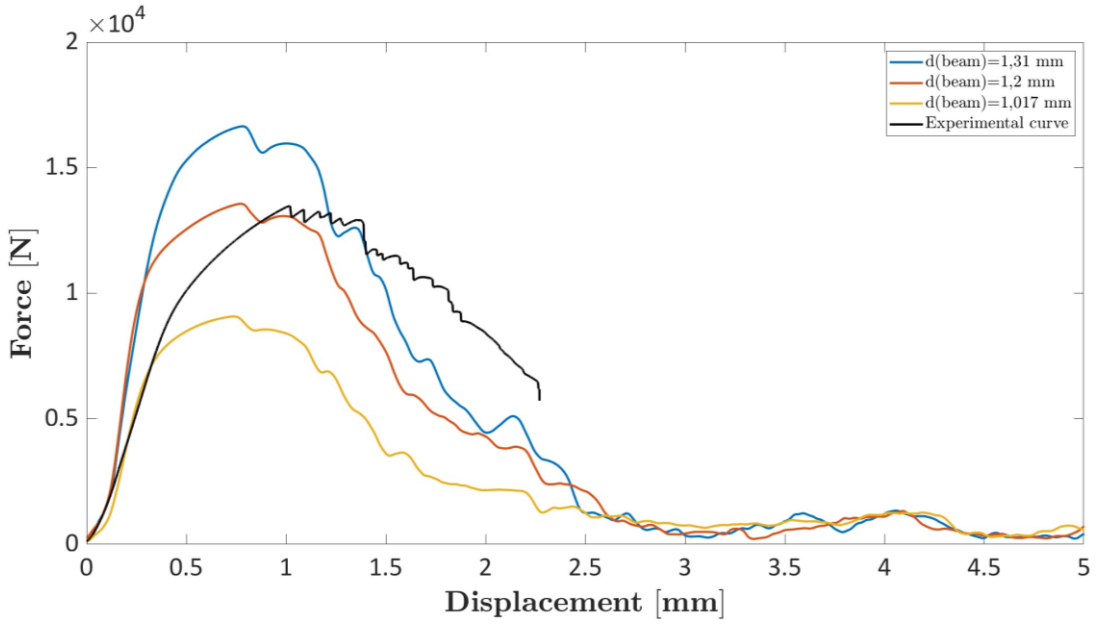

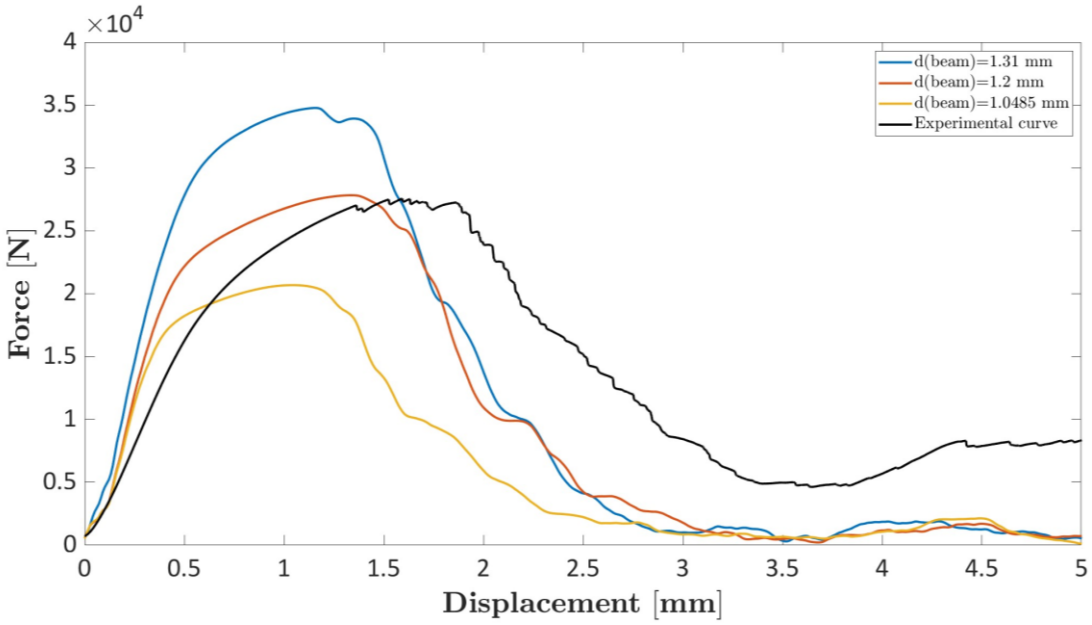

Figure 6.8 Determination of the effective beam diameter d=1.2 mm and the corresponding Force-Displacement curve obtained (red curve). The upper graph corresponds to the 20 x 20 mm cell, while the lower graph corresponds to the 30 x 30 mm cell

Regarding the peak force reached, the numerical model achieves values comparable to the experimental behavior in both specimens. Therefore, the calibration performed on the 20 x 20 mm cell is considered validated for the 30 x 30 mm cell.

However, the numerical curve (red) still does not provide a wholly acceptable approximation of the experimental behavior, especially concerning the load descent phase following the fracture of the first beams. Consequently, to calibrate the model correctly, it was necessary to adjust the *fail* parameter. This parameter represents the plastic strain at failure for the stress-strain curves of the RVEs with defects, which are included as MATERIAL CARD in the numerical model in Ls-Dyna.

In order to achieve proportional control for all defect classes, it was chosen to vary all fail values uniformly by using a unique multiplicative factor. This sensitivity study led to good approximation results using a multiplicative factor of **2** for both simulations on the 20 x 20 mm and 30 x 30 mm cells (Figure 6.9).

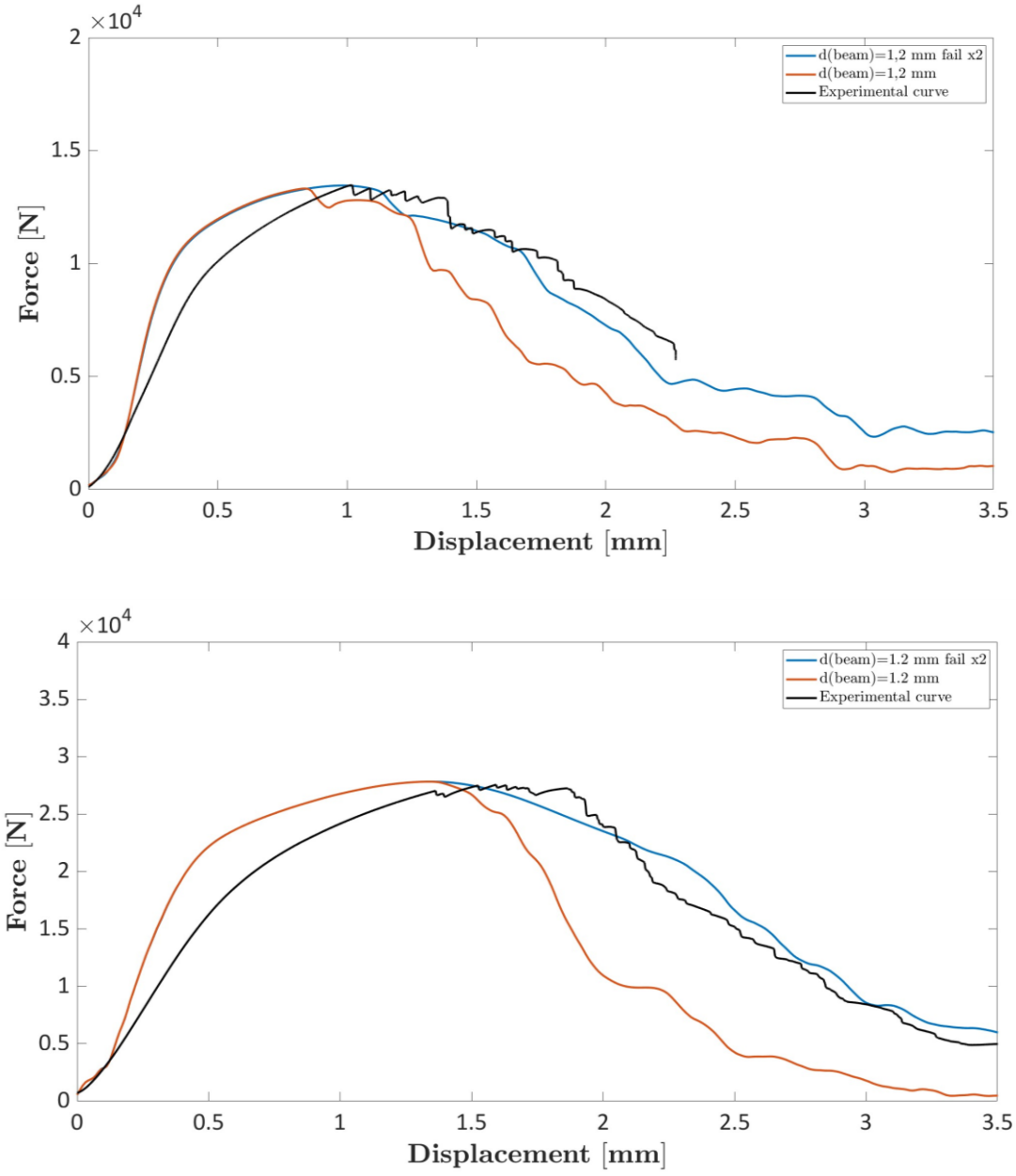

Figure 6.9 Determination of the FAIL parameter achieving the best approximation (blue curve) of the experimental curve. The upper graph corresponds to the 20 x 20 mm cell, while the lower graph corresponds to the 30 x 30 mm cell

Once the calibration parameters for the numerical model were determined, the influence of internal defects was introduced. Seven tests were then conducted for both the 20 x 20 mm and 30 x 30 mm cells, varying the association of MATERIAL CARD to mesh elements proportionally to the defect distribution. This approach allowed obtaining a family of force-displacement numerical curves with a certain variability dictated by the defect distribution in the model.

Figures 6.10 and 6.11 present the results obtained for the lattice specimen with 20 x 20 mm and 30 x 30 mm cells, respectively. Compared to the case without defects, these new simulations show a reduction in stiffness in the elastic region, which better approximates the experimental case. In both cases, the peak force achieved slightly decreases compared to simulations without defects.

It can also be noted that the random insertion of defects influences only the load descent section with variability, while all curves maintain the same trend, and thus equal stiffness, in the elastic range.

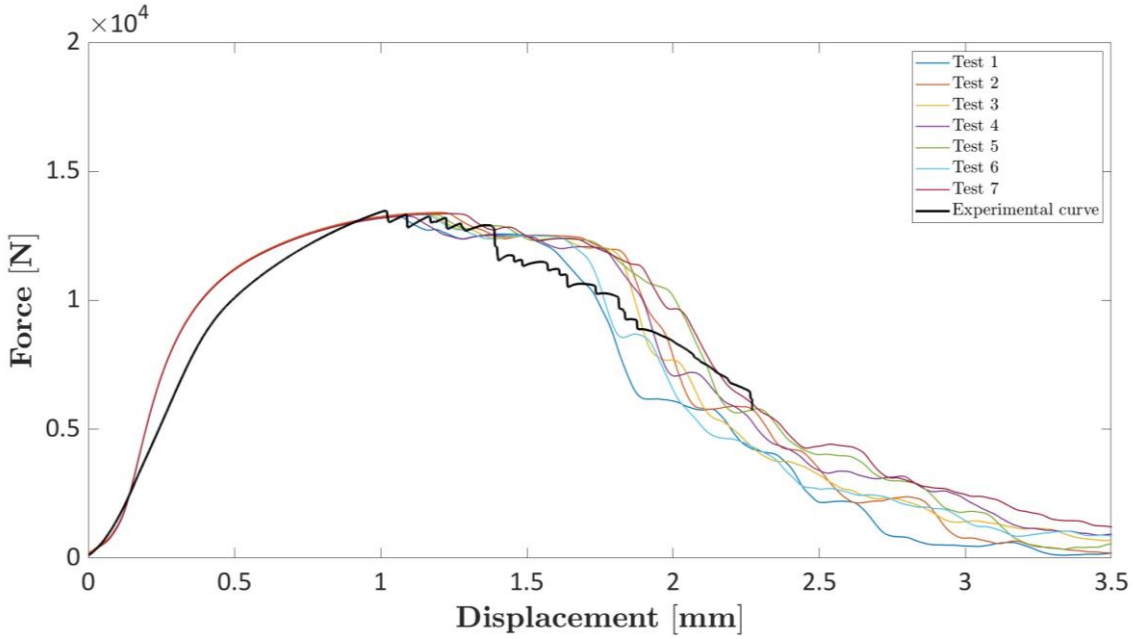

Figure 6.10 Numerical test curves with internal defects and comparison with the experimental curve. Case with a 20 x 20 mm cell

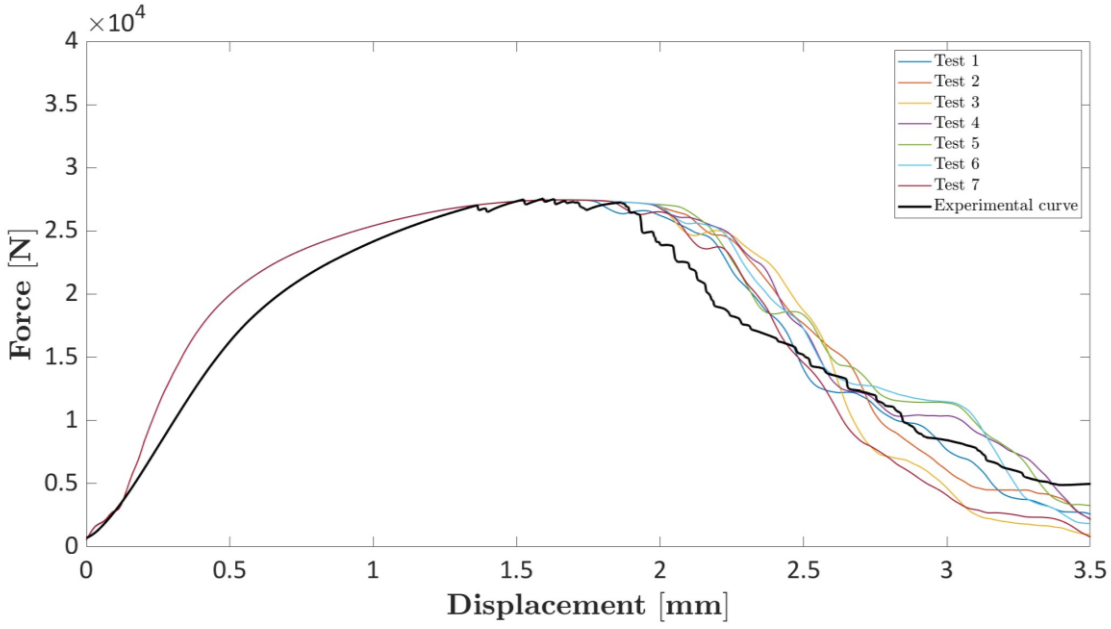

Figure 6.11 Numerical test curves with internal defects and comparison with the experimental curve. Case with a 30 x 30 mm cell

With the information obtained from these tests, the next step was to define an overall variability range of numerical results, useful for design purposes. To achieve this, a MATLAB script was developed. Given the numerical curves obtained from the FE analysis as input, the script calculates an average curve μ and the standard deviation σ for each point.

Assuming that the numerical curves follow a Gaussian normal distribution, two upper and lower limit curves were determined to contain at least 95% of the values, according to the probability given by the Gaussian distribution:

$$95\% = P\{ \mu - 1{,}96\,\sigma < X < \mu + 1{,}96\,\sigma \} \qquad (6.1)$$

The calculated average curve and the band between the upper and lower limit curves are shown in Figure 6.12.

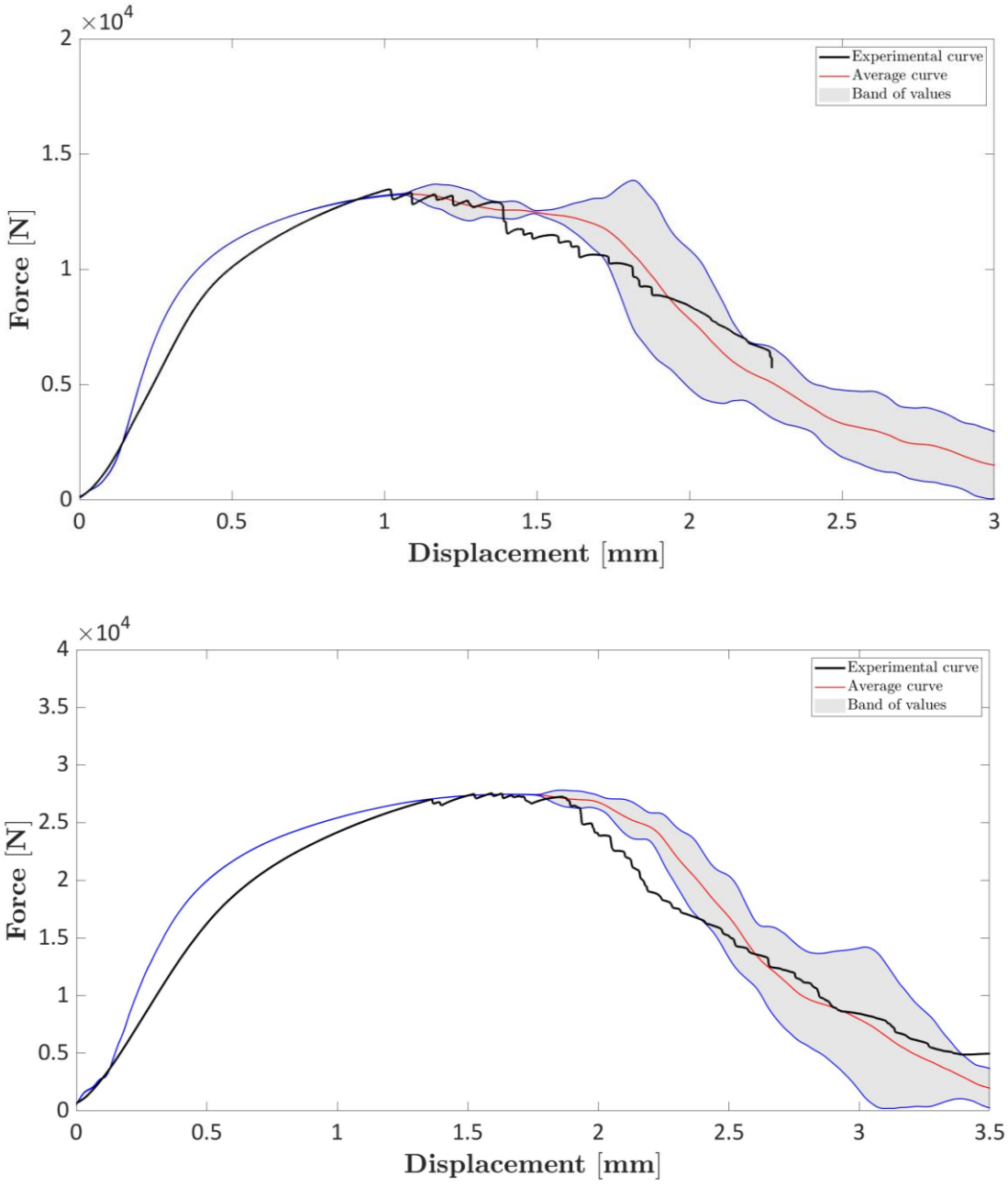

Figure 6.12 Determining the band of numerical curves and comparison with the experimental curve. The upper graph corresponds to the 20 x 20 mm cell, while the lower graph corresponds to the 30 x 30 mm cell

Once the validity band was established, it was necessary to determine a force-displacement curve to use as a reference during the design phase. The objective of this final step in the study was to obtain a general curve to be associated with a defect-free lattice specimen model. This curve could then be used in the FEM

design of lattice structures without having to incorporate actual defects into the model.

For this purpose, the lower limit curve of the band was considered as the reference curve for the design (Figure 6.13).

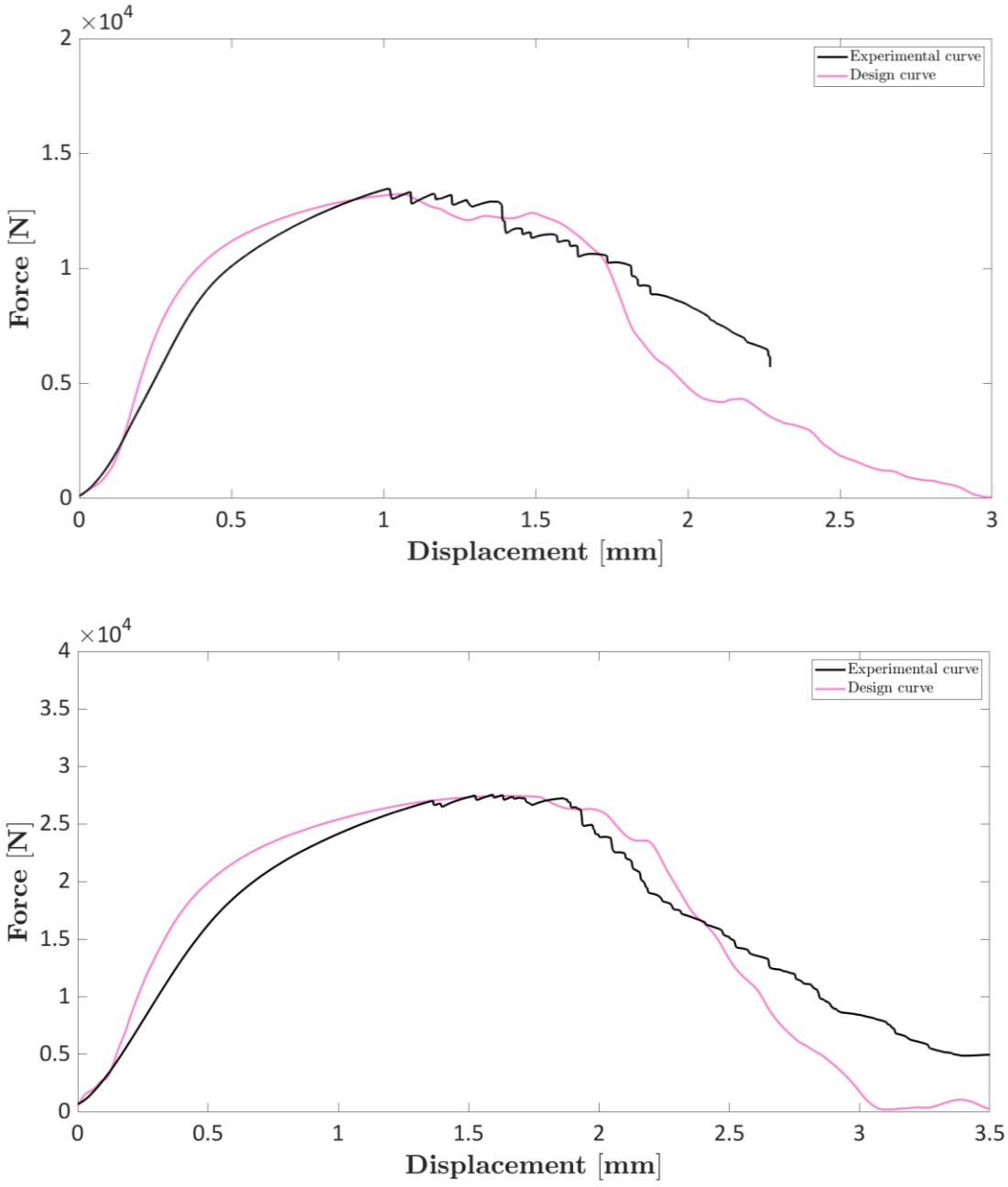

Figure 6.13 Comparison between the experimental curve and the design numerical curve. The upper graph corresponds to the 20 x 20 mm cell, while the lower graph corresponds to the 30 x 30 mm cell

Conclusions

In conclusion, this thesis work has enabled the definition of a finite element numerical model to simulate and predict the static compression behavior of lattice structures produced through Additive Manufacturing. Experimental tests were initially conducted on the lattice cell, along with Micro Computed Tomography scans that revealed the presence of internal defects due to the manufacturing process.

Subsequently, data related to material properties, geometric characteristics, and the distribution of internal defects were used as inputs for creating the model using a multiscale approach. A representative volume element (RVE) at the local scale was defined with the same properties of the initial model, incorporating internal defects in the form of spherical cavities. These analyses led to the selection of a cylindrical RVE for assessing the optimal results in terms of stress-strain curves.

The material response curves on the RVE were then defined as Material Cards at the macroscale, with a random association proportional to the defect distribution between the material cards and the beam elements of the lattice specimen model.

Finite Element Analysis (FEA) simulations on the lattice structure model generated force-displacement curves, which were then compared with experimental behavior. Although a higher stiffness in the elastic range of the numerical model compared to the experimental one was observed, satisfactory approximation results were obtained, defining a validity range for the numerical results.

The lower limit of the range was then considered as a design curve for potential defect-free specimen FE models. A limitation of the study is that the model

considers only the influence of internal defects in the beams, while analyzing the impact of surface roughness on mechanical strength could be beneficial.

Subsequent studies could focus on a more in-depth analysis of the x, y, z position of the spherical cavity within the RVE. It has been observed that variability in both the radius and the elevation of the defect influences the maximum stress reached in the RVE at the time of the first mesh element failure.

Further development involves exploiting the use of Machine Learning algorithms to ensure a faster estimation of the mechanical behavior of the lattice structure based on the defect distribution. Specifically, machine learning algorithms are a set of techniques that allow computers to learn from data and adapt automatically without being explicitly programmed. These algorithms can be trained using input data such as component geometry, process parameters, and material properties. They can analyze and learn patterns present in the data to create predictive models for mechanical behavior.

The use of ML algorithms for simulating the mechanical behavior of components produced through Additive Manufacturing can lead to significant advantages, such as reducing development times and costs, optimizing performance, and rapidly exploring and evaluating various design solutions.

Therefore, by implementing a Machine Learning algorithm appropriately trained with the stress-strain datasets of the already obtained RVEs, it would be possible to predict the mechanical behavior in the presence of new defects without having to perform new FE simulations.

Appendix

Python function for extracting stress-strain data from Abaqus CAE odb file.

```
def extract_data_from_odb(odb_path, output_file):
    odb = openOdb(odb_path)

    first_step_name = next(iter(odb.steps.keys()))
    step = odb.steps[first_step_name]
    with open(output_file, 'a') as file:
        file.write(
            "        Stress                Strain
Elastic Modulus                Max Element Strain \n")

    outer_loop = False
    for frame_index in range(1, len(step.frames)):
        last_frame = step.frames[frame_index]
        first_frame = step.frames[-1]

        stress_field = last_frame.fieldOutputs['S']
        strain_field = last_frame.fieldOutputs['E']
        volume_field = last_frame.fieldOutputs['EVOL']

        stress_components = ['S11', 'S22', 'S33', 'S12', 'S23', 'S13']

        # Specify the stress component and consequently the strain
component that you want to extract
        component = 'S11'
        element_data = {}
        av_strain_vec = []

        count_label = 0
        for element in odb.rootAssembly.instances['CUBE-1'].elements:
            element_label = element.label
            count_label += 1

        print(count_label)

        count = 0
```

```
        for element in odb.rootAssembly.instances['CUBE-1'].elements:
            element_label = element.label

            stress =
stress_field.getSubset(region=element).values[0].data[stress_component
s.index(component)]
            strain =
strain_field.getSubset(region=element).values[0].data[stress_component
s.index(component)]
            volume =
volume_field.getSubset(region=element).values[0].data

            average_stress = np.mean(stress)
            average_strain = np.mean(strain)

            # mark the elements that exceed the ultimate strain at
each frame
            if count < count_label * 0.0005: #define the threshold
percentage of elements at failure
                av_strain_vec.append(average_strain)

                if average_strain < -0.1:
                    count += 1
                    print('Elements at failure %d' % count)
                    print(element_label)

            else:
                outer_loop = True
                break

            element_data[element_label] = {
                'Average Stress': average_stress,
                'Average Strain': average_strain,
                'Element Volume': volume
            }

        if outer_loop:
            print('max reached')
```

```
            break

        total_volume = sum([data['Element Volume'] for data in
element_data.values()])
        total_stress = sum(
            [data['Average Stress'] * data['Element Volume'] for data
in element_data.values()]) / total_volume
        total_strain = sum(
            [data['Average Strain'] * data['Element Volume'] for data
in element_data.values()]) / total_volume
        max_strain = min(av_strain_vec)

        elastic_modulus = total_stress / total_strain

        with open(output_file, 'a') as file:
            for element_label, data in element_data.items():
                average_stress = data['Average Stress']
                average_strain = data['Average Strain']
                volume = data['Element Volume']

            file.write("         {}         {}              {}
{}\n".format(total_stress, total_strain,

elastic_modulus, max_strain))
    with open(output_file, 'a') as file:
        file.write("Total Model Volume: {}\n".format(total_volume))
    odb.close()
```

References

[1] https://gen3d.com/news-and-articles/types-of-lattices-for-additive-manufacturing/

[2] M. F. Ashby, «The properties of foams and lattices», Philosophical Transactions of the Royal Society A: Mathematical, Physical and Engineering Sciences, 2005.

[3] Tobias Maconachie, Martin Leary, Bill Lozanovski, Xuezhe Zhang, Ma Qian, Omar Faruque, Milan Brandt, «SLM lattice structures: Properties, performance, applications and challenges», RMIT Centre for Additive Manufacture, RMIT University, Melbourne, Australia, 2019.

[4] Vinh Phu Nguyen, Martijn Stroeven, Lambertus Johannes Sluys, «Multiscale continuous and discontinuous modelling of heterogeneous materials»,Delft University of Technology, Faculty of Civil Engineering and Geosciences, 2012.

[5] Ivano Benedetti, «BEMs for Multiscale Materials Modelling including damage and failure», Turin Polytechnic University, 2023.

[6] George Z. Voyiadjis * and Mohammadreza Yaghoobi, «Review of Nanoindentation Size Effect: Experiments and Atomistic Simulation», Computational Solid Mechanics Laboratory, Department of Civil and Environmental Engineering, 2017.

[7] «Weidong Wu, Joseph Owino, «Applying Periodic Boundary Conditions in Finite Element Analysis»,Applying Periodic Boundary Conditions in Finite Element Analysis

[8] M. Suard, G. Martin, P. Lhuissier, R. Dendievel, F. Vignat, J.-J. Blandin, F. Villeneuve, «Mechanical equivalent diameter of single struts for the stiffnessprediction of lattice structures produced by Electron Beam Melting», Univ. Grenoble Alpes, France, 2015.

Aknowledgements

I would like to first thank Prof. Andrea Tridello, the supervisor of this thesis, for always guiding me with kindness and dedication, providing support through guidance and advice throughout the project.
Alongside him, I want to express my gratitude to my co-supervisors: Prof. Alberto Ciampaglia, Prof. Carlo Boursier Niutta, and Prof. Davide Salvatore Paolino for their constant availability at every stage of the work and for the valuable teachings they have imparted to me.

I want to extend my thanks to my family, to whom I owe so much. To my parents and my sister: without you, without your support, I would never have reached this milestone. I am grateful because you have never let me lack anything and have always encouraged me to pursue my dreams and passions.

A special thank you to my girlfriend, Silvia. Thank you for believing in me and always showing me the bright side of things. Thanks for supporting me, reassuring me during anxieties and difficulties, but also for all the joys and silly moments we've shared. Thank you for always being there.

I would also like to express my gratitude to my great friends Matteo and Stefano for all the company and laughter over the years, for the inevitable video calls during the week.
Thanks also to my roommate Bruno for all the beautiful moments and adventures lived in Turin over the last two years.

Finally, a big thank you to the Magia group, my old friends, and the new people i have met in Turin. I hope these friendships can last forever.

Ringraziamenti

Vorrei per prima cosa ringraziare il prof. Andrea Tridello, relatore del presente lavoro di tesi, per avermi sempre seguito con gentilezza ed impegno, attraverso le guide e i consigli, per tutta la durata del progetto.
Insieme a lui desidero ringraziare anche i miei co-relatori: prof. Alberto Ciampaglia, prof. Carlo Boursier Niutta e prof. Davide Salvatore Paolino per tutta la disponibilità in ogni step del lavoro e per gli insegnamenti che mi hanno trasmesso.

Desidero poi ringraziare la mia famiglia a cui devo tanto. Ai miei genitori e a mia sorella: senza di voi, senza il vostro sostegno non sarei mai arrivato a raggiungere questo traguardo. Vi sono grato perché non mi avete mai fatto mancare niente e mi avete sempre incoraggiato a portare avanti i sogni e le passioni.

Un rigraziamento speciale alla mia fidanzata Silvia. Grazie per aver creduto in me e per avermi sempre fatto vedere il bicchiere mezzo pieno delle cose. Grazie per avermi supportato, per avermi tranquillizzato durante le ansie e le difficoltà, ma anche per tutte le gioie e i momenti stupidi insieme. Grazie perché ci sei sempre stata.

Un grazie anche ai miei grandi amici Matteo e Stefano per tutta la compagnia e le risate in questi anni, per le videochiamate immancabili durante la settimana. Grazie anche al mio coinquilino Bruno per tutti i bei momenti e le avventure vissute a Torino in questi ultimi due anni.
Infine un grazie al gruppo Magia, a tutti i miei amici di casa e alle nuove persone che ho conosciuto a Torino, spero che queste amicizie possano continuare per sempre.